

# Simulations of Mars Rover Traverses

Feng Zhou, Raymond E. Arvidson, and Keith Bennett

Department of Earth and Planetary Sciences, Washington University in St Louis, St Louis, Missouri 63130

e-mail: chow@wunder.wustl.edu, arvidson@wunder.wustl.edu, bennett@wustl.edu

Brian Trease, Randel Lindemann, and Paolo Bellutta

California Institute of Technology/Jet Propulsion Laboratory, Pasadena, California 91011

e-mail: brian.p.trease@jpl.nasa.gov, randel.a.lindemann@jpl.nasa.gov, bellutta@helios.jpl.nasa.gov

Karl Iagnemma and Carmine Senatore

Robotic Mobility Group Massachusetts Institute of Technology, Cambridge, Massachusetts 02139

e-mail: kdi@mit.edu, senator@mit.edu

Received 7 December 2012; accepted 21 August 2013

Artemis (Adams-based Rover Terramechanics and Mobility Interaction Simulator) is a software tool developed to simulate rigid-wheel planetary rover traverses across natural terrain surfaces. It is based on mechanically realistic rover models and the use of classical terramechanics expressions to model spatially variable wheel-soil and wheel-bedrock properties. Artemis's capabilities and limitations for the Mars Exploration Rovers (Spirit and Opportunity) were explored using single-wheel laboratory-based tests, rover field tests at the Jet Propulsion Laboratory Mars Yard, and tests on bedrock and dune sand surfaces in the Mojave Desert. Artemis was then used to provide physical insight into the high soil sinkage and slippage encountered by Opportunity while crossing an aeolian ripple on the Meridiani plains and high motor currents encountered while driving on a tilted bedrock surface at Cape York on the rim of Endeavour Crater. Artemis will continue to evolve and is intended to be used on a continuing basis as a tool to help evaluate mobility issues over candidate Opportunity and the Mars Science Laboratory Curiosity rover drive paths, in addition to retrieval of terrain properties by the iterative registration of model and actual drive results. © 2013 Wiley Periodicals, Inc.

## 1. INTRODUCTION

Mars robotic rovers have included Sojourner Truth as part of the Pathfinder Mission in 1997 (Golombek et al., 1997), the two Mars Exploration Rovers (MER), Spirit and Opportunity, which landed in January 2004 (Squyres et al., 2004a,2004b), and the Mars Science Laboratory's Curiosity rover, which landed on August 5, 2012 (Grotzinger et al., 2012). The ability to traverse laterally and acquire detailed remote sensing and in situ observations has proven to be of immense value for exploration and discovery [see the mission summaries in Arvidson et al. (2006,2008,2010,2011a); Grotzinger et al. (2013); and Squyres et al. (2006)]. On the other hand, the Martian terrain has occasionally presented significant challenges to autonomous roving to scientifically interesting targets. For example, the Spirit rover, with its inoperative right front wheel, became embedded in deformable sands near the eroded volcano Home Plate (Arvidson et al., 2010). In addition, Opportunity has been subjected to several near-embedding events when it traversed into deformable sands associated with wind-blown ripples on the

plains of Meridiani (Arvidson et al., 2011a). Curiosity will have to traverse relatively steep slopes (up to 20°) to reach its targeted outcrops on Mount Sharp, and some traverses will likely involve significant soil sinkage and slip, combined with slip and skid over bedrock outcrops (Arvidson et al., 2013).

Realistic simulations of rover-terrain interactions during traverses are needed to help engineers define safe and efficient paths to waypoints for robotic systems such as Opportunity and Curiosity. A spin-off of such a capability is that the rover can also be used as a virtual instrument, sensing the terrain slope distributions, together with soil and bedrock properties. Registration of model and flight data can be used to retrieve surface properties and also increase the confidence with which future traverse path options can be simulated. To that end, the authors have completed initial development of a software package called Artemis (Adams-based Rover Terramechanics and Mobility Interaction Simulator) using validated mechanical models for Spirit, Opportunity, and Curiosity, and realistic topography, soil properties, and bedrock characteristics. Classical wheel-soil interactions are modeled for deformable soils, along with standard frictional contacts between wheels and bedrock. The intent in this paper is to build upon the

Direct correspondence to: Feng Zhou, e-mail: chow@wunder.wustl.edu

initial development work on Artemis reported in Trease et al. (2011) and Iagnemma et al. (2011), including evaluating capabilities and limitations of the current models using Earth-based laboratory and field tests, and a discussion of example applications for simulating drives for Opportunity. The paper ends with a look forward to additional development and validation efforts and use of Artemis to systematically simulate drives for Opportunity and Curiosity, including retrieval of terrain properties.

## 2. ARTEMIS DEVELOPMENT AND VALIDATION APPROACHES

As reported in Trease et al. (2011) and Iagnemma et al. (2011), initial work on Artemis began with use of a mechanically realistic Mars Exploration Rover (MER) that was developed in MSC Corporation's MSC-Adams (Automatic Dynamic Analysis of Mechanical Systems) and validated for MER drop tests (Lindemann, 2005; Lindemann & Voorhees, 2005; Lindemann, Bickler, Harrington, Ortiz, & Voorhees, 2006). For Artemis the authors added simulations of drive actuators for the wheels and interactions between the driven rover and realistic terrains derived from flight data for both Spirit and Opportunity. This included use of digital elevation maps (DEMs) generated from the rover-based Panoramic (Pancam) and Navigational (Navcam) cameras on the masts, and estimates of soil and bedrock properties for each cell location within the DEMs. An issue was how to model soil and bedrock interactions with the MER wheels, and the choices included finite element models (e.g., Fervers, 2004; Yong & Fattah, 1976), discrete element models (Horner, Peters, & Carrillo, 2001; Knuth, Johnson, Hopkins, Sullivan, & Moore, 2012; Tsuji et al., 2012), and use of classical terramechanics models [based on Bekker's original work for deformable soils (see, e.g., Bekker, 1960,1969)] for deformable soils and simple Coulomb frictional contact models for bedrock (Cameron, Jain, Huntsberger, Sohl, & Mukherjee, 2009; Dupont & Yamajako, 1997; Kraus, Kumar, & Dupont, 1998; Sohl & Jain, 2005). The authors chose the latter two approaches to model interactions between the wheels, soil, and bedrock, as appropriate, largely because Artemis needed to run quickly for use in tactical path planning. In addition, the MERs have rigid wheels and travel very slowly (i.e., the wheel surface interactions are quasistatic), consistent with assumptions used in the classical models. Finally, a great deal of work had already been done on use of these relatively simple yet powerful terramechanics modeling approaches for single-wheel systems and even rovers. Before detailing the approaches used in developing the Artemis model for the MERs, key previous work is summarized in the next few paragraphs. Note that a Curiosity model has also been developed and tested in Artemis and will be the subject of a separate publication.

For deformable soils, the classical methods of terramechanics are based on pressure-sinkage relationships derived

from bevameter flat plate experiments for soil deformation, combined with shear box experiments that provide information on shear displacement as a function of applied shear stress under a specified normal stress (Bekker, 1960,1969; Janosi & Hanamoto, 1961; Wong & Reece, 1967a,1967b). These expressions are then mapped to cylindrical wheel geometries to determine the normal and shear stresses as a function of position for a wheel of a specified radius. Numerous references exist for this approach and its modifications, and the equations have been reproduced in dozens of papers. The reader is referred to Wong (2001,2010) for concise summaries of the approaches. The effect of grousers has also been included by a number of workers (Bauer, Leung, & Barfoot, 2005; Ding, Yoshida, Nagatani, Gao, & Deng, 2009; Watyotha, Gee-Clough, & Salokhe, 2001; Wong, 2001), as has the influence of bulldozing of soil along the drive or longitudinal direction (Bekker, 1969; Hegedus, 1960; Ishigami, 2008; Richter et al., 2006), and the effects of wheel sidewall resistance (Del Rosario, 1980; Schwanghart, 1968). Wheel-soil laboratory tests have been conducted by numerous researchers, testing variants of the terramechanics expressions, and results indicate that the classical terramechanics expressions are valid for a wide range of wheel sinkage ( $<1/2$  wheel radii) (Bauer et al., 2005) and slippage ( $<80\%$ ) (Ishigami, 2008; Scharringhausen, Beermann, Krömer, & Richter, 2009).

As shown in subsequent sections of this paper, Artemis builds on previous terramechanics results to model wheel-soil stresses in longitudinal and lateral directions. Some commercial software packages were found that incorporated the classical terramechanics models for deformable soils, such as the Soft Soil Tire Model (AS2TM, 2003) and the MSC-Adams Soft-Soil Tire Model (Adams online help, 2012). These models integrate the normal and shear stresses as a function of position within the contact areas between the wheels and soils, although details of the approaches were lacking. To ensure a thorough understanding of the interaction approaches, Artemis uses standard wheel-soil interaction models, including longitudinal and lateral stresses and wheel-soil geometries on tilted or otherwise irregular terrains, developed in software by the authors. Specifically, the Artemis single-wheel-soil interaction algorithm is in part based on work presented in Scharringhausen et al. (2009), who implemented a numerical approach to integrate stresses over the wheel-soil contact patch area, with model validation using single-wheel test-bed data for a spare MER flight wheel. To deal with sloped terrains, the approach adopted was previously used by Yoshida and his group (Inotsume, Sutoh, Nagaoka, Nagatani, & Yoshida, 2012; Ishigami, 2008; Ishigami, Miwa, Nagatani, & Yoshida, 2006,2007; Yoshida, Watanabe, Mizuno, & Ishigami, 2003), who applied classical terramechanics equations on tilted surfaces using modified wheel-soil contact angles for stress calculations. Again, their model was validated using rover test-bed experiments as part of their research.

Wheel-bedrock interaction models for slowly moving rovers with rigid wheels proved to be much simpler to implement in Artemis relative to wheel-soil interactions. The wheel-bedrock contact model is based on elastic interactions with minimal penetration of the wheel into the bedrock and stress distributions dominated by static and dynamic coefficients of friction (Adams online help, 2012; Dupont & Yamajako, 1997; Kraus et al., 1998; Song, Kraus, Kumar, & Dupont, 2000). As shown in subsequent sections of this paper, the MSC Adams standard contact model for mobility systems replicated key drives at the Jet Propulsion Laboratory's Mars Yard and the Tecopa bedrock outcrops in the Mojave Desert, and this model was thus incorporated into Artemis.

The next step in the development of Artemis was to model the rover mechanical system with its six-wheel drive capabilities as it drove over realistic terrains that incorporated DEMs and spatially variable deformable soil properties. Krenn and Hirzinger (2008,2009) and Schäfer, Gibbesch, Krenn, and Rebele (2010) developed and tested numerical methods using classical terramechanics equations for rover-scale models. The authors closely followed the work of these authors in developing the Artemis rover model for deformable soils. For the bedrock or contact model, MSC Adams already included contact detection and calculation between rigid bodies, and thus Artemis development efforts for the contact model were straightforward and limited to population and ingestion of the relevant DEMs.

A number of approaches were used to validate the Artemis models for driving across realistic terrains with deformable soils or bedrock outcrops, as appropriate. First, at the single-wheel model level a series of experiments were conducted with a spare MER wheel at the MIT Robotic Mobility Group Laboratory and compared to Artemis results. Soil mechanical properties were in part fixed using bevameter and shear box tests for the soil simulants used in the experiments. Second, numerous traverse trials were done at the Jet Propulsion Laboratory's Mars Yard in Altadena, CA, a roughly football field sized area covered with soils exposed on varying slopes, together with bedrock plates arranged with varying tilts. Most of these tests were done without extensive instrumentation to determine wheel sinkage or slippage and thus the main purpose was to gain experience in how the MER test rovers responded to varying slopes and surface properties. These tests proved to be invaluable for showing how the vehicles negotiated, for example, changes in slope values as they moved from horizontal to tilted surfaces. Third, detailed tests were conducted in the Dumont Dunes areas of the Mojave Desert with the MER test rovers, including determination of wheel sinkages and rover-based slippage as a function of dune face slopes. As part of this deployment, the rover also traversed tilted and benchlike bedrock outcrops in the Tecopa region of the Mojave Desert. Fourth, two of the authors (R.E.A. and P.B.) have been involved in MER and Curiosity drive planning

and analysis of the downlink data on almost a daily basis and have a great deal of experience in how the three rovers behaved while traversing flat and irregular surfaces covered by deformable soils and by bedrock. This experience base proved to be important in determining whether Artemis properly models the response of the rovers to specific terrains.

### 3. ARTEMIS DESCRIPTION AND ASSUMPTIONS

As noted, Artemis was developed using MSC-Adams as the multibody dynamics simulation engine (MSC Software, 2012). Artemis consists of a rover mechanical model, a wheel-terrain interaction model, and terrain, bedrock, and soil models. Terrain surfaces are modeled using the Surface and Topography Preprocessor (Figure 1). Bedrock and soil parameters and wheel configurations are defined in the Terrain and Configuration file. The Wheel-terrain Contact Module is used to detect wheel-terrain contacts, including the entry/exit angles and sinkages for deformable soil, and penetration and contact points for bedrock. It is also used to define the relationship between the wheel local coordinate frame and the rover global coordinate frame. The conversion between these two frames is used to define wheel kinematic information for further wheel-terrain interaction calculations.

As noted, for bedrock the Artemis model employs the classical Coulomb friction contact expressions included in MSC-Adams to calculate wheel-bedrock interactions. For deformable soils, Artemis uses the Wheel-soil Interaction Module to calculate forces, stresses, and torques using classical terramechanics equations. In both cases, calculated values are fed back to the Adams/Solver to implement the drive simulations. A Rover Motion Control Module is used to simulate rover drive commands. Simulation results can then be examined using the Adams/Postprocessor. The details of the modeling approaches are presented in the following sections.

#### 3.1. MER Rover Model

The MERs are six-wheel drive, four-wheel steered vehicles with a rocker-bogie suspension system (Lindemann & Voorhees, 2005). A 200-element Adams mechanical model of the rover was developed and validated before launch using MSC-Adams dynamic modeling software (Lindemann & Voorhees, 2005; Lindemann et al., 2006). The original model, which was developed as a high-fidelity representation of the rover structure, mass, and stiffness properties, did not include the active (e.g., actuators) and passive (e.g., free pivots) mechanisms needed to simulate mobility. Thus, new efforts were started as part of Artemis to simulate active wheel driving, steering actuators, and passive mechanisms such as hard-stops on the joint pivots. The final rover model used in Artemis includes 85 moving

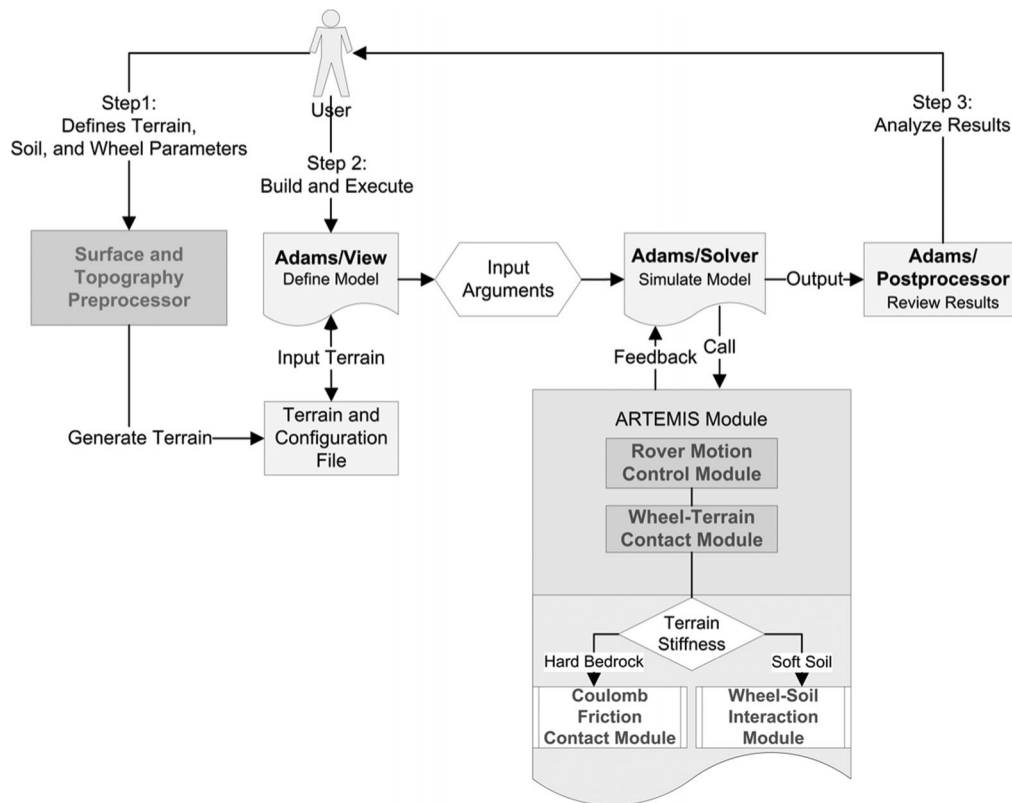


Figure 1. Artemis architecture.

individual parts or rigid bodies. The rigid bodies, representing the distributed and lumped masses of the rover, are connected to one another in the structure by massless beam elements. The rigid bodies are connected by revolute or pin joints. These revolute joints have the mechanism functions for actuator torques, friction losses, and mechanical stops. More rover details can be found in (Lindemann, 2005; Lindemann & Voorhees, 2005; Lindemann et al., 2006).

Artemis uses motion statements to control driving and steering actuator rotational angles and speeds. The motion statements are formulated to replicate drive commands sent to the MER or Curiosity rover on Mars. The motion statements are implemented by customizing the Adams/Solver motion subroutine and are encapsulated in the Rover Motion Control Module. The rover model is able to simulate straight drives and arc turns, including blind drives and drives using visual odometry (visodom) to simulate course corrections to reach waypoints (Cheng, Maimone, & Matthies, 2006; Maimone, Cheng, & Matthies, 2007). Further, the model includes Spirit's failed drive actuator on its right front wheel. It also includes Opportunity's failed steering actuator on the right front wheel, which became permanently immobilized while rotated inward by  $8^\circ$  early in the mission. The Curiosity version of Artemis likewise uses motion controls to implement its drive simulations,

and this model is also built on a validated mechanical model in MSC Adams used for drop tests.

### 3.2. Wheel-bedrock Contact Model

Artemis considers the wheel-bedrock contact model as a solid-to-solid dynamic frictional contact. The contact model included in Adams/Solver is utilized and, as noted, has been utilized in previous planetary rover studies (Benamar & Grand, 2013; Cowan & Sharf, 2007; Lindemann, 2005; Tao, Deng, Fang, Gao, & Yu, 2006). Adams/Solver models the contact as a unilateral constraint, that is, contact force has a positive value when penetration exists between two contact geometries and otherwise it has zero value (Adams online help, 2012). As shown in Eq. (1), the contact normal force between the wheel and bedrock is modeled as a non-linear spring-damper with stiffness and viscous damping components:

$$F_n = kz^e + c_d \dot{z} \quad (1)$$

where  $k$  is the stiffness between the rigid wheel and underlying bedrock,  $z$  represents the penetration of one contact geometry into another,  $e$  specifies the exponent of the force-deformation characteristic,  $c_d$  is the damping coefficient between the two contact materials for penetration  $z$ ,

and  $\dot{z}$  is the time derivative of  $z$ . The stiffness component is proportional to  $k$  and is a function of the penetration. The stiffness component opposes the penetration. The damping component is a function of the speed of penetration. The damping opposes the direction of relative motion. Given the low speed of the rover and its wheels, the effect of the damping coefficient is not significant. The damping coefficient achieves a maximum,  $c_{max}$ , at a user-defined penetration  $z_{max}$ . For a given penetration,  $z$ , the corresponding damping coefficient,  $c_d$ , is determined by the Heaviside step function of  $c_{max}$ ,  $z_{max}$ , and  $z$ .

The Adams/Solver uses a relatively simple velocity-based friction expression to model dynamic friction based on Coulomb friction (Adams online help, 2012). The coefficient of friction,  $\mu$ , is determined by the Heaviside step function with a cubic polynomial based on specified parameters (Adams online help, 2012). These parameters include the stiction transition velocity  $v_{st}$ , the friction transition velocity  $v_{ft}$ , the static friction coefficient  $\mu_s$ , and the dynamic friction coefficient  $\mu_d$ . The coefficient of friction  $\mu$  is calculated using

$$\mu(v) = \begin{cases} \text{step}(|v|, -v_{st}, \mu_s, v_{st}, -\mu_s) & (\text{if } v \leq v_{st}) \\ -\text{sign}(v) \cdot \text{step}(|v|, v_{ft}, \mu_d, v_{st}, \mu_s) & (\text{if } v_{st} \leq |v| \leq v_{ft}) \\ -\text{sign}(v) \cdot \mu_d & (\text{if } v_{ft} \leq |v|) \end{cases} \quad (2)$$

The friction force is then calculated using the calculated coefficient of friction  $\mu$  and normal force  $F_n$  from Eq. (1). If the Adams/Solver detects an angular velocity about the contact normal axis, it will apply a torque proportional to the friction force. The contact friction torque is calculated using

$$T_f = \frac{2}{3} r_c F \quad (3)$$

where  $r_c$  is the radius of the contact area (for rigid body contact,  $r_c$  is the wheel radius),  $F$  is the friction force, and  $2/3$  is the coefficient used in Adams/Solver from Marks' Standard Handbook for Mechanical Engineers (Adams online help, 2012).

The wheel-bedrock contact is treated as a contact between solid to solid. The penetration between them is quite limited since both the wheel and the bedrock are rigid bodies. Details about the contact detection algorithm are included in Section 3.4.2.

### 3.3. Wheel-soil Interaction Model

The Artemis wheel-soil interaction model follows the discretization approach developed by Scharringhausen et al. (2009). Figure 2 illustrates the possible stresses along all directions. Using the methods developed by Krenn and Hirzinger (2008,2009) and Schäfer et al. (2010), the wheel is treated as a three-dimensional (3D) mesh and is divided into many small cells along both longitudinal and lateral

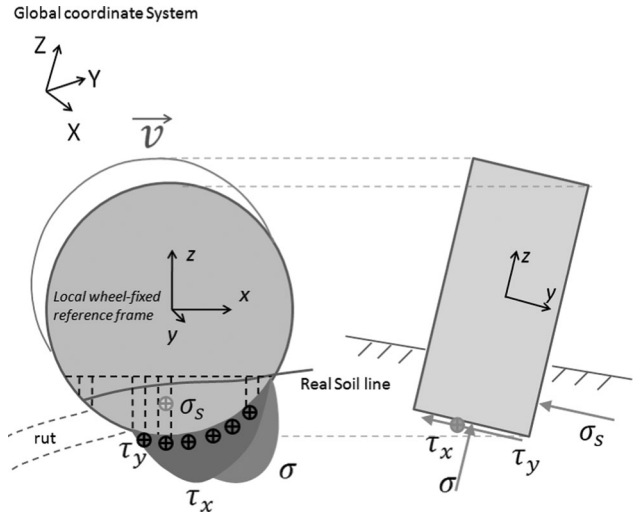


**Figure 2.** Illustration of stresses along the wheel-soil contact interface. Normal stress ( $\sigma$ ) and longitudinal shear stress ( $\tau_x$ ) distributions are shown.  $\tau_y$  is the lateral shear stress and  $\sigma_s$  is the passive soil pressure acting on the wheel sidewall.

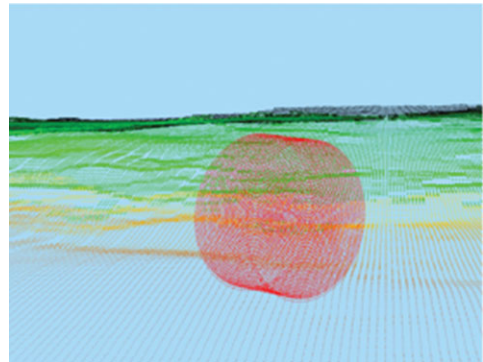


**Figure 3.** Illustration of the three-dimensional wheel mesh and terrain digital elevation model.

directions to provide fine resolution for numerical integrations between the wheel and soil needed to define stress distributions (Figure 3). The terrain surface is modeled as a digital elevation model in which each cell is assigned deformable soil parameters. The calculation of stresses between the wheel and deformable soil is described in later sections.

#### 3.3.1. Calculation of Slip and Slip-sinkage

Longitudinal wheel slip is a kinematic measure of the relative motion between a wheel and the underlying terrain. The slip value determines the amount of traction that a wheel is able to develop. In Artemis, the following equation is used to calculate wheel slip (positive/driving) and skid

(negative/braking),  $i$ , for bedrock and soil:

$$i = \begin{cases} 1 - \frac{v}{r\omega} & (\text{if } v < r\omega \text{ driving}) \\ \frac{r\omega}{v} - 1 & (\text{if } v > r\omega \text{ braking}) \end{cases} \quad (4)$$

where  $v$  is the wheel's forward velocity,  $\omega$  is the wheel's angular velocity, and  $r$  is the wheel's radius. Slip values range from  $-1$  to  $1$  with a limiting case of zero longitudinal velocity and therefore slip =  $1$ , whereas for negative slip the limiting case is zero angular velocity and therefore slip =  $-1$ . For Opportunity, rover-based slip values are calculated by comparing the rover's actual traveled distance against the theoretical distance (as if there was no slip) using visual odometry techniques (Maimone et al., 2007).

Wheel slip often results in excavation of soil around the wheel, leading to downward wheel displacement, which is termed slip-sinkage. An expression that linearly relates the sinkage exponent to the slip ratio is adopted to calculate the slip-sinkage in Artemis for deformable soil (Ding, Gao, Deng, & Tao, 2010a; Ding et al., 2009,2010b):

$$n = n_0 + n_1 |i| \quad (5)$$

where  $n_0$  is the nominal sinkage exponent and  $n_1$  is the slip-sinkage exponent, which is determined empirically. Other models to calculate slip-sinkage have been proposed by several researchers (e.g., Lyasko, 2010; Muro & O'Brien, 2004). For example, Muro and O'Brien (2004) modeled the slip-sinkage as an additional sinkage caused by contact pressure and slippage. This model requires knowledge of three coefficients, which have to be determined experimentally for a given wheel-soil characteristics. Since the contact pressure and slippage are different at each contact point, the calculated slip-sinkage is the sum of each element slip-sinkage amount. Comparing these two methods, Eq. (5) is more direct and convenient and thus was adopted in Artemis.

### 3.3.2. Normal Stress Calculations

Normal stresses at the wheel-soil contact patch are assumed to be purely radial and are approximated using the pressure-sinkage relationship based on Bekker's equation (Wong & Reece, 1967a,1967b):

$$\sigma(\theta) = \begin{cases} \left(\frac{k_c}{b} + k_\phi\right) (r)^n (\cos \theta - \cos \theta_f)^n & \theta_m < \theta < \theta_f \\ \left(\frac{k_c}{b} + k_\phi\right) (r)^n \left(\cos \left(\theta_f - \frac{\theta - \theta_r}{\theta_m - \theta_r} (\theta_f - \theta_m)\right) - \cos \theta_f\right)^n & \theta_r < \theta < \theta_m \end{cases} \quad (6)$$

or Reece's equation (Reece, 1965; Wong, 2001,2012):

$$\sigma(\theta) = \begin{cases} (ck'_c + \rho gbk'_\phi) \left(\frac{r}{b}\right)^n (\cos \theta - \cos \theta_f)^n & \theta_m < \theta < \theta_f \\ (ck'_c + \rho gbk'_\phi) \left(\frac{r}{b}\right)^n \left(\cos \left(\theta_f - \frac{\theta - \theta_r}{\theta_m - \theta_r} (\theta_f - \theta_m)\right) - \cos \theta_f\right)^n & \theta_r < \theta < \theta_m \end{cases} \quad (7)$$

where  $\theta_f$  is the soil entry angle,  $\theta_r$  is the exit angle, and  $\theta_m$  is the angle at which the maximum normal stress occurs. Parameters  $k_c$ ,  $k_\phi$ ,  $n$ ,  $k'_c$ ,  $k'_\phi$ ,  $c$ , and  $\rho$  depend on soil properties,  $r$  and  $b$  correspond to the wheel radius and the smaller dimension of the contact patch, respectively, and  $g$  is gravitational acceleration. Wheel width is used as the smaller dimension of the contact patch in Artemis. The pressure-sinkage parameters in Reece's equation,  $k'_c$  and  $k'_\phi$ , can be derived from pressure-sinkage parameters in Bekker's equation,  $k_c$  and  $k_\phi$ , for a given  $n$  and  $b$ . Reece's equation, although similar to Bekker's equation (the two produce exactly matching results for the same  $b$  value), is dimensionally correct in the sense that  $k'_c$  and  $k'_\phi$  are truly nondimensional parameters. Also, Reece's equation explicitly accounts for gravitational acceleration, terrain cohesion,  $c$ , and soil mass density,  $\rho$ . Both sets of equations are available in Artemis.

Equations (6) and (7) were developed for horizontal soil surfaces. For sloped surfaces, the approach used by Yoshida et al. (2003) and others (Ding et al., 2010b; Inotsume et al., 2012; Ishigami et al., 2006,2008) is adopted for Artemis. Normal and shear stresses at the wheel-soil contact are computed by resolving the gravity vector relative to the slope. Stresses are then calculated using Eqs. (6) and (7) with modified contact angles. Figure 4 illustrates the normal stress distribution along the wheel-soil contact interface on a tilted surface. The entry angle is based on the original terrain elevation and the exit angle is based on the deformed terrain elevation. All contact angles are based on the wheel local frame to handle tilted surfaces. Soil strength may be affected by slope angle. However, given the moderate soil-covered slopes ( $\leq 15^\circ$ ) traversed by Opportunity, the effect is not significant.

The location of  $\theta_m$  is important to estimate the normal stress distribution. According to Oida's experiments,  $\theta_m$  changes with slip and can be expressed as a polynomial function of slip (Oida, Satoh, Itoh, & Triratanasirichai, 1991). If the higher-order items are ignored, Oida's equation is the

Global coordinate System

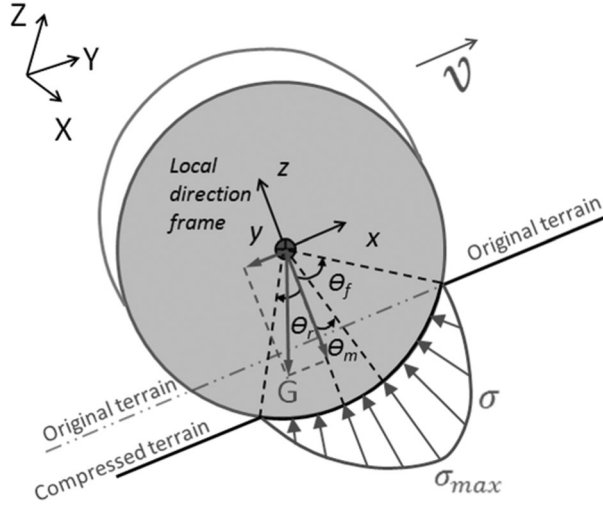


**Figure 4.** Illustration of normal stress along the wheel-soil contact interface. Entry angle ( $\theta_f$ ) and exit angle ( $\theta_r$ ) are both in the wheel local frame, as is  $\theta_m$ , the central angle of maximum normal stress ( $\sigma_{max}$ ).

same as Wong's equation (Wong & Reece, 1967a):

$$\theta_m = (a_1 + a_2 i) \theta_f \quad (8)$$

where  $i$  is the wheel slip, and  $a_1$  and  $a_2$  are two model parameters. Wong and Reece (1967b) suggested a different formula of  $\theta_m$  for skid. Use of that formula creates discontinuity issues around zero slip because of the sudden change of the calculated  $\theta_m$  during the transition from slip to skid or reverse. Thus only Eq. (8) is used in Artemis. Parameters  $a_1$  and  $a_2$  are treated as tuning parameters.

### 3.3.3. Shear Stress Calculations

Shear stresses in the longitudinal direction (direction of travel) are the primary source of driving traction. The shear stress estimation used in Artemis is based on a widely used empirical formula first proposed by Janosi and Hanamoto (1961):

$$\tau_x(\theta) = \tau_{max} \left(1 - e^{-\frac{j_x}{k_x}}\right) \quad (9)$$

where  $\tau_{max}$  is the maximum shear stress,  $j_x$  is the shear displacement, and  $k_x$  is the shear deformation modulus. According to the Mohr-Coulomb failure criterion,  $\tau_{max}$  can be related to normal stress as

$$\tau_{max} = c + \sigma(\theta) \tan \phi \quad (10)$$

where  $c$  is cohesion and  $\phi$  is the internal friction angle. Shear displacement  $j_x$  of an arbitrary point can be calculated by integrating tangential slip velocity from time

0 to the arbitrary time  $t$  as shown in Eq. (11) (Wong & Reece, 1967a):

$$j_x = \int_0^t v_x dt = \int_{\theta}^{\theta_f} v_x \frac{d\theta}{\omega} = \int_{\theta}^{\theta_f} \{r\omega - v \cos \theta\} \frac{d\theta}{\omega} \quad (11)$$

where  $v_t$  is the tangential slip velocity,  $v$  is the wheel's forward velocity,  $\omega$  is the wheel's angular velocity, and  $r$  is the wheel's radius. Considering the slip definition given in Eq. (4), Eq. (11) yields (Wong & Reece, 1967a):

$$j_x = \begin{cases} r(\theta_f - \theta - (1-i)(\sin \theta_f - \sin \theta)) & i \geq 0 \\ r\left(\theta_f - \theta - \frac{(\sin \theta_f - \sin \theta)}{i+1}\right) & i < 0 \end{cases} \quad (12)$$

During turning maneuvers (or any motion that induces lateral wheel slip), lateral shear stresses arise and can be calculated in a similar fashion as the longitudinal shear stresses (Schwanghart, 1968; Ishigami et al., 2007):

$$\tau_y(\theta) = (c + \sigma(\theta) \tan \phi) \left(1 - e^{-\frac{j_y}{k_y}}\right) \quad (13)$$

$$j_y = \int_0^t v_y dt = \int_{\theta}^{\theta_f} v_y \frac{d\theta}{\omega} \quad (14)$$

where  $k_y$  is the lateral shear deformation modulus, which is assigned as the same value of  $k_x$  in Artemis, and  $v_y$  is the lateral velocity of the wheel and is related to the forward velocity:

$$v_y = v \tan \beta \quad (15)$$

where  $\beta$  is the lateral slip angle and  $v$  is the wheel's forward velocity. Figure 5 shows the relationship between longitudinal and lateral velocity from the wheel's top view. The lateral slip angle is the angle between the wheel's true moving direction and the longitudinal axis of the wheel. Integrating Eq. (14), a similar form to Eq. (12) yields (Ishigami, 2008)

$$j_y = \begin{cases} r(1-i)(\theta_f - \theta) \tan \beta & i \geq 0 \\ \frac{r(\theta_f - \theta) \tan \beta}{(1+i)} & i < 0 \end{cases} \quad (16)$$

### 3.3.4. Bulldozing, Sidewall Resistance, and Grouser Forces

The authors chose to ignore bulldozing forces because soil is not seen bulldozed in front (i.e., in the drive direction) of Spirit, Opportunity, or Curiosity wheels according to the Hazcam, NavCam, and PanCam images covering the rover wheel tracks (See Section 4).

When lateral slip occurs, resistance occurs at the wheel sidewall as shown in Figure 5. The sidewall resistance is based on the Terzaghi bearing capacity (Terzaghi, Peck, & Mesri, 1996) and the Hettiaratchi-Reece equations (Hettiaratchi & Reece, 1967) for a wall moving into a mass of soil. It was adopted for the first time by Schwanghart (1968) to model the ground resistance on the sidewall of a tire embedded in soil. We are using Schwanghart's approach to

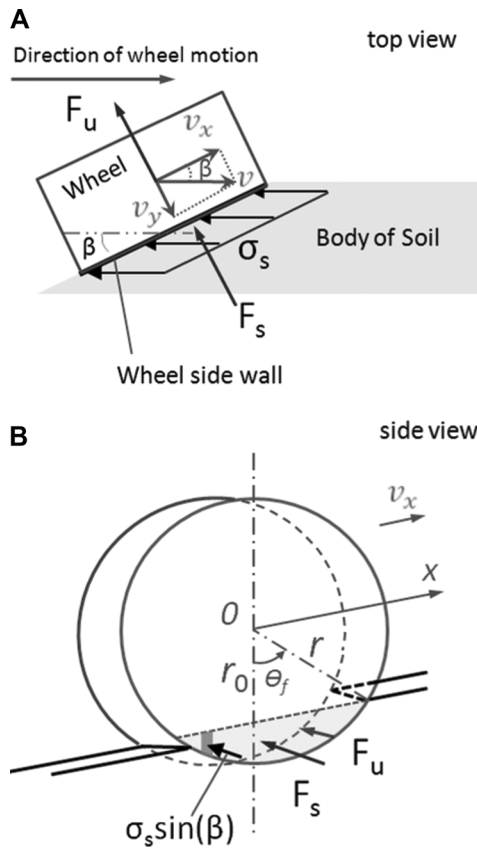


**Figure 5.** Illustration of lateral forces.  $\beta$  is the slip angle,  $v_x$  is the longitude velocity and  $v_y$  is lateral velocity,  $F_u$  is the lateral shear force underneath the wheel, and  $F_s$  is the sidewall resistance.

model this lateral force:

$$\sigma_s = \gamma z N_\gamma + c N_c + q N_q \tag{17}$$

$$N_\gamma = \frac{2(N_q + 1) \tan \phi}{1 + 0.4 \sin(4\phi)}, \quad N_c = \frac{N_q - 1}{\tan \phi},$$

$$N_q = \frac{e^{(1.5\pi - \phi) \tan \phi}}{2 \cos^2(\pi/4 + \phi/2)} \tag{18}$$

where  $\sigma_s$  is the passive soil pressure caused by compacting side soil,  $\gamma$  is the soil weight density,  $z$  is the sinkage of a given point,  $\phi$  is the internal friction angle,  $q$  is the surcharge (additional pressure on the soil, for example, caused by the accumulated bulldozed soil), and  $c$  is the cohesion.  $N_\gamma$ ,  $N_c$ ,  $N_q$  are modified Terzaghi parameters from Coduto (2001). Integrating the lateral component of  $\sigma_s$  along the wheel sidewall leads to the calculation of sidewall resistance:

$$F_s = \sin \beta \int_{-r \sin \theta_f}^{r \sin \theta_f} \{ \gamma N_\gamma f(x) + c N_c + q N_q \} f(x) dx \tag{19}$$

where  $f(x) = (\sqrt{r^2 - x^2} - r_0)$ ,  $r_0 = r \cos \theta_f$ ,  $\theta_f$  is the entry angle,  $\beta$  is the slip angle, and  $r$  is wheel radius. Equation (19) has not been experimentally validated and may not be appropriate for high sinkages and slip angles. For results presented in this paper, these limitations are not relevant since lateral dynamics were minimal for the drives that were simulated.

Both the MER and MSL rover wheels include grousers to increase traction. At the MIT Robotic Mobility Group Laboratory, the MER wheel produced larger drawbar pull (net tractive force) than a smooth wheel with the same outer diameter under the same test condition. (For example, the MER wheel has 30% more drawbar pull than the smooth wheel under 20% imposed slip and 135 N vertical load.) Therefore, it was decided to explicitly include grouser influences in Artemis.

The force acting on each grouser ( $F_g$ ) for deformable soils is shown in Figure 6. By assuming that the grouser surface is smooth and thus there is no friction between the grouser and the soil (therefore the soil-grouser friction angle is zero), the grouser force with zero vertical inclination angle can be modeled in Eq. (20) based on the equations in Wong (2001):

$$F_g = b \left( \frac{1}{2} \rho g h_b^2 N_\phi + q h_b N_\phi + 2 c h_b \sqrt{N_\phi} \right) \tag{20}$$

where  $\rho$  is the soil mass density,  $g$  is gravitational acceleration,  $h_b$  is the height of the grouser,  $q$  is surcharge,  $c$  is cohesion,  $N_\phi = \tan^2(\pi/4 + \phi/2)$  is a constant about the internal friction angle  $\phi$ , and  $b$  is the grouser width. For a grouser with a vertical inclination angle  $\beta_b$  as shown in Figure 6, a similar equation is used (Wong, 2001):

$$F_g = b \left( \frac{1}{2} \rho g h_b^2 K_{p\gamma} + q h_b K_{pq} + c h_b K_{pc} \right) \tag{21}$$

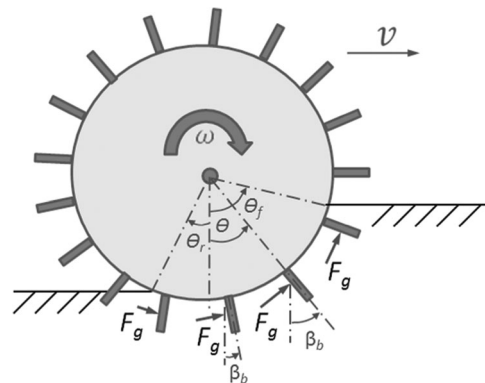


**Figure 6.** Tractive forces due to wheel grousers (cleats), where  $\theta$  is the central angle of a given grouser,  $F_g$  is the soil reaction on a given grouser, and  $\beta_b$  is the vertical inclination angle of a given grouser.

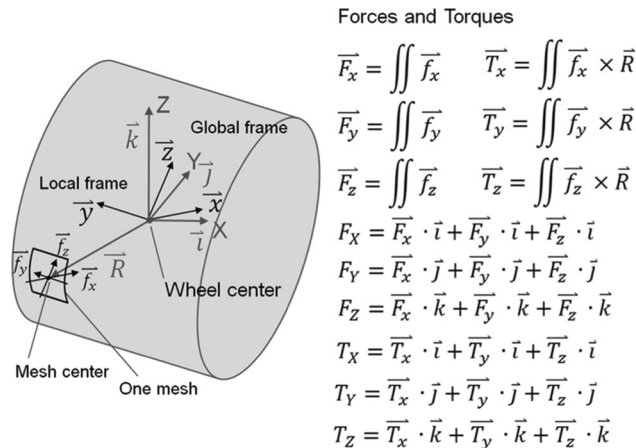


**Figure 7.** Illustration of forces and torques calculation (where  $F_X, F_Y, F_Z, T_X, T_Y, T_Z$  are forces and torques along each axis in a global frame).

where

$$K_{py} = N_\phi \cos \beta_b, \quad K_{pq} = N_\phi, \quad K_{pc} = 2\sqrt{N_\phi}$$

As shown in Figure 6, the force acting on each grouser in Artemis is decomposed into two directions according to the central angle  $\theta$ . The sum of the two components contributes to the tractive and normal forces. Each grouser force acts at  $\sim 2/3$  length of grouser height for torque calculation. The total grouser forces are the sum of the individual grouser forces for the grousers in contact with soil. The in-contact grousers are determined during simulation by the Contact Detection Module, including the location and central angle of each in-contact grouser. The summation of total grouser forces is then based on Eqs. (20) and (21) for the grousers in contact with soil. The total grouser force increases with the number of in-contact grousers as long as they are separate enough to engage soil independently. This is true for MER wheels, which have 31 grousers per wheel. The height of the grousers is 6 mm and the width is 16 cm. Usually there are only two to four grousers in contact with soil, given a sinkage of 2–3 cm. Note that the surcharge used in Eqs. (19)–(21) was set to zero in the simulations since bulldozing was not observed in MER drives.

### 3.3.5. Force and Torque Calculations

Based on methods presented in Schäfer et al. (2010), the stresses for each mesh cell are integrated to provide a single set of forces at the wheel center (Figure 7). First,  $f_x, f_y, f_z$ , the element forces in one contact patch along the wheel local frame directions, are calculated based on stresses in this patch. Then the element forces are summed together. For torques, the element forces in the local frame are multiplied by the moment arm length and then are summed together. All calculations are performed in the wheel lo-

cal frame and then transformed to the rover global frame. Forces and torques are decomposed along each axis of the wheel local frame and then combined together to calculate six values (along three axes). These local forces and torques are then decomposed and combined again along the rover global frame. The decomposition follows the 3D transformation between the two frames. The conversion between two frames depends on the wheel location and orientation. Finally, the summed 3D forces and torques are input into Adams for dynamic calculations. The sidewall resistance and grouser forces, calculated separately, are also added to the summation of forces and torques.

## 3.4. Terrain Modeling

In this section, modeling of the terrain topography and properties is discussed, along with wheel-surface contacts, positionally dependent soil properties, and modeling multiple wheel passes through soil.

### 3.4.1. Surface Model and Terrain Properties

In Artemis, digital elevation models consisting of discrete cells are used to represent the terrain (including spatially dependent soil properties), whereas wheels are modeled as 3D meshes. The surface cell size is typically  $\sim 1$  cm, whereas wheel mesh size is usually  $\sim 0.05$  cm. The size of the mesh and terrain cell size can be adjusted externally in the Terrain and Configuration file generated in the Artemis Surface and Topography Preprocessor (Figure 1). The Terrain and Configuration file contains the needed terrain information including elevation values and soil or bedrock properties as well as the wheel information. Digital terrain models used in Artemis range from simple tilted planes to actual elevation models derived from orbital or rover-based stereo images.

### 3.4.2. Contact Detections

Wheel-terrain contacts are estimated using the Wheel-terrain Contact Module, which, as noted, was adopted from work done by Krenn and Hirzinger (2008,2009) and Schäfer et al. (2010). This procedure finds the portions of the wheel mesh that are below the undeformed soil surface and computes contact angles from the center of the wheel to the wheel-soil contact locations. Wheel sinkage is computed based on the deepest penetration of the wheel into the soil. The exit angle is calculated based on the assumption presented in Ishigami et al. (2007) that the soil rebounds by some model-dependent amount after being compressed. For tilted surfaces, the reference zero central angle axis is perpendicular to the tilted surface and pointing downward (Figure 3). The entry and exit angles are then referenced to this axis (Ishigami, 2008). The number of grousers in contact with the soil is determined in a similar way by comparing

the elevation of the grouser end point and the corresponding soil cell.

New elevation values are used to update the in-contact cells based on the sinkage and soil rebound ratio after wheels have passed over the cell. These new values are also used to create the imprint information for display of tracks and to generate a deformed soil shell.

Contacts between wheel and bedrock are based on the detection algorithm implemented in the Adams/Solver for solid-to-solid contacts. After contact occurs between two solids, the Adams/Solver computes the volumes of intersection and assumes that the intersection between two solids will be much less than the volume of either solid. This is accurate for rigid bodies. Adams then finds the center of mass of the intersection volume (assuming the intersection volume has uniform density) and the closest point on each solid to the centroid. The distance between these two points is the penetration depth.

### 3.4.3. Multiple Soils and Multipass Modeling

Multiple soils are modeled by allowing the soil terramechanics properties to vary as a function of location within the terrain model. For the contact model, the scene is assumed to be homogeneous in terms of bedrock properties.

The multipass effect occurs when a leading wheel deforms the soil and a subsequent wheel enters the soil and further deforms it. Previous research has shown that the impact of the first pass is greater than subsequent passes (Abebe, Tanaka, & Yamazaki, 1989; Holm, 1969). Observations of Spirit, Opportunity, and Curiosity's wheel tracks also show the vast majority of deformable soil deformation is due to the first wheel pass (see Section 4). The relationship between sinkage after the  $n$ th pass and the one after the first pass can be modeled by Eq. (22) according to (Scholander, 1974)

$$Z_{np} = Z_1 \cdot n_p^a \quad (22)$$

where  $n_p$  is the number of passes,  $Z_{np}$  is the total sinkage after  $n_p$  pass,  $Z_1$  is the sinkage after the first pass, and  $a$  is the multipass coefficient. According to Abebe et al. (1989),  $a$  is 2 to 3 for loose soils and low loads; it is set as 3 in Artemis. The soil density after  $n_p$  pass is modeled as a function of the number of passes and the slip of the first pass, following the work of Senatore and Sandu (2011):

$$\gamma_n = \gamma_0 (k_1 + k_2 n_p) \quad (23)$$

where  $\gamma_0$  is the weight density of undisturbed soil,  $n_p$  is the number of passes,  $\gamma_n$  is the density of soil after  $n_p$  passes,  $k_1$  is a slip-related coefficient, and  $k_2$  is a constant. Cohesion after  $n_p$  passes follows the same trend as in Eq. (23) (Senatore & Sandu, 2011). The values of  $k_1$  and  $k_2$  are determined as a function of slip and the number of passes based on the pressure-sinkage relationship in Eq. (22).

To implement the multipass effect, a set of record-booking approaches is used in Artemis to record relationships between the wheels and cells and the status of soil regions actively involved in a wheel pass. These records are used to update the deformed soil properties after each pass.

### 3.5. Artemis Drive Simulator

On Mars, rover traverses are performed through blind drives and autonomous navigation (autonav) drives (Biesiadecki et al., 2006; Biesiadecki, Leger, & Maimone, 2007). Blind drives are the Ackermann arc drives from a starting position to a waypoint target in which the rover tracks its orientation but calculates its distance traveled based on wheel odometry, assuming zero wheel slip. It corrects its course to the waypoint periodically during its traverse with the aforementioned assumption of zero slip. Autonav drives use stereo-based tracking (visual odometry, or visodom) of terrain targets to correct course deviations based on both orientation and actual distance traversed (Cheng et al., 2006). Figure 8 illustrates how Ackermann arcs are implemented by varying wheel angular velocities to implement an arc with a given radius of curvature.

Artemis simulates both blind and autonav drives. To simulate autonav drives, Artemis uses internal rover pose data for positions in which commanded visual odometry stations were obtained to update traverses to waypoints. In addition, Artemis simulates a turn-in-place drive, which is an arc-turn that rotates the vehicle without lateral motion. Artemis models these drives using the Rover Motion Control Module (Figure 1).

### 3.6 Artemis Single-wheel Model

Artemis also includes a single-wheel option to compare to laboratory experiments focused on wheel-soil interactions. The single-wheel model uses the same wheel-terrain

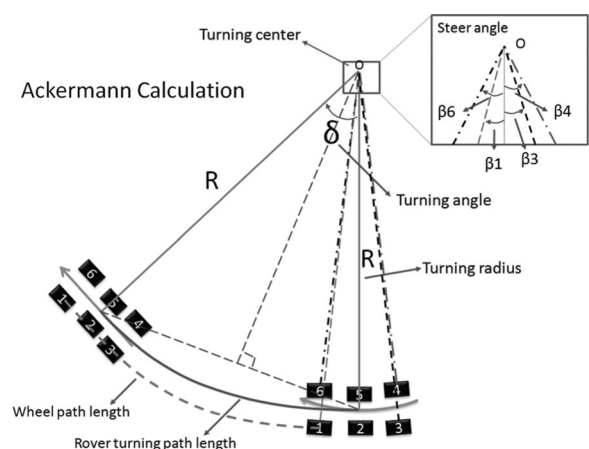


Figure 8. Ackermann drive illustration.

interaction model as the full version of Artemis. Self-propelled (i.e., free slip) wheel and propelled wheel (i.e., imposed slip) simulations are both supported.

#### 4. ARTEMIS VALIDATION RESULTS

In this section, validation of the Artemis models is presented, including single-wheel model comparisons to laboratory data, comparisons of full rover models and field data, and comparisons of model and Opportunity flight data.

##### 4.1. Single-wheel Experiments in Deformable Soil

As noted in Section 2, single-wheel deformable soil experiments were conducted at the MIT Robotic Mobility Group Laboratory using a MER spare flight wheel (13.1 cm radius and 16 cm width) within a confined soil bin of dimensions 1.5 m long, 0.7 m wide, and 0.4 m deep (Figure 9; Senatore, Wulfmeier, MacLennan, Jayakumar, & Iagnemma, 2012). A six-axis force torque transducer was mounted between the wheel mount and the carriage to measure the vertical load and traction generated by the driven wheel. Finally, a flange-to-flange reaction torque sensor was used to measure driving torque applied to the wheel. Runs were made with constant slippage under applied vertical loads of 100 and 135 N, values that cover the range of expected loads for the MER wheels on Mars. Drawbar pull (the net tractive force), rolling torque (the torque applied to the wheel to move at constant angular velocity), and wheel sinkage were measured as a function of load and imposed slips ranging up to 0.6. The upper slip bound was chosen based on maximum slip reported for Opportunity's drives (Arvidson et al., 2011b).

The test-bed soil consisted of Mojave Martian Simulant, which is composed of loose, poorly sorted basaltic sands (Peters et al., 2008). The simulant bulk density was determined using standard laboratory procedures. The parameters  $k_c$ ,  $k_\phi$ ,  $n$ , needed to establish the pressure sinkage relationship [see Eq. (6)] were determined based on bevameter tests using 160-mm-long and 25-, 50-, and 75-mm-wide plates. Soil cohesion,  $c$ , internal friction angle,

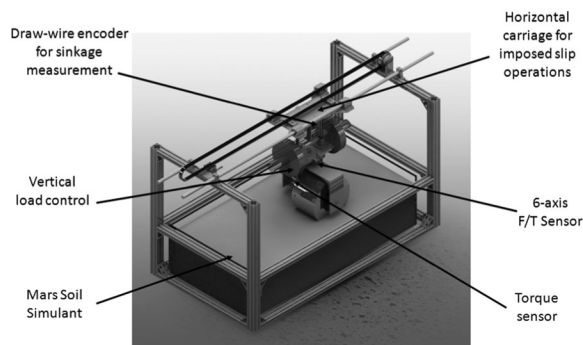


Figure 9. MIT single-wheel test bed.

$\phi$ , and shear deformation modulus,  $k_x$  [see Eq. (9)], were determined from shear box tests with applied normal stress values ranging from 2 to 50 kPa (Senatore & Iagnemma, 2011). Inferred values for soil parameters from the density, shear box, and bevameter measurements are listed in Table I, along with  $a_1$  and  $a_2$  from Eq. (8) needed to determine contact angles,  $n_1$ , the second pressure-sinkage exponent for modeling slip-sinkage dynamics [Eq. (5)], and, finally, the soil rebound ratio. These latter four variables were not independently measured in the laboratory and were used as parameters to adjust or tune to have Artemis model results conform to test results.

Initial results showed that the nominal model values in Table I poorly replicated the data trends, and varying the tuning parameters did not allow the model to conform to the data. Model sensitivity tests showed that the value of  $k_x$  (0.60 mm) inferred from shear box data was far too small to produce reasonable model results. The final value for  $k_x$  is well within values for soils quoted in the literature (e.g., Wong, 2001) but certainly not the small value obtained from the shear box tests. A number of Artemis models were run with the addition of  $k_x$  as a tuning parameter, and a chi-square approach was used to determine the best combined fits for drawbar pull, torque, and sinkage as a function of load and imposed slip. These values are reported in Table I and correspond to a chi-square  $P$  value with less than a 5% chance of rejection for the entire range of data and model results. Figure 10 shows the test data and best-fit Artemis models using the final parameters shown in Table I. The error bars displayed in these plots are test standard deviations based on the ten runs per imposed slip values.

As shown in Figure 10, the sinkage estimates have large standard deviations, and this is a consequence of the inability to prepare the surface back to its original topographic state after each run. Even so, the model and data conform as a function of normal load for varying imposed slip values, including the trend of increasing sinkage with increasing imposed slip. Torque and drawbar pull values with increasing imposed slip show concave downward trends in both data and model fits. The importance of slip-sinkage is also evident, as is the decrease in drawbar pull with high slip values. The models do overestimate torque at high and underestimate drawbar pull at low imposed slip values. No combination of parameter values was found that would better fit the data throughout the entire range of imposed slips. Similar results have been found by other researchers (Ishigami, 2008; Richter et al., 2006; Scharringhausen et al., 2009), indicating a limitation in the classical terramechanics equations. Exploration of model parameter space indicates that the expressions for the angular location of maximum normal stress [Eq. (8)] and the second sinkage exponent [Eq. (5)] are the primary causes of the lack of fit to the entire range of imposed slip data. The implication for use of Artemis is that care must be taken when registering model and flight data, and the model in its current form will

**Table I.** Measured and estimated Mars Mojave Simulant soil parameters.

	$\rho$	$c$	$\phi$	$k'_c$	$k'_\phi$	$n(n_0)$	$n_1$	$k_x$	$a_1$	$a_2$	Rebound
units	kg/m <sup>3</sup>	kPa	deg	-	-	-	-	mm	-	-	-
Starting values	1550	0.6	35	677.5	212.2	1.4	0.54	0.6	0.33	0.11	3%
Final values	1550	0.6	35	677.5	212.2	1.4	0.354	14.6	0.365	0.503	7%

Note:  $n_1$  initial value from Ding et al. (2009);  $a_1, a_2$  from Oida et al. (1991); and sinkage parameter  $k'_c$  and  $k'_\phi$  are converted from measured bevameter test-bed soil parameters based on  $n = 1.4, b = 0.16$  m, and  $\rho = 1550$  kg/m<sup>3</sup>.

provide physical insight into drive results with retrieval of terrain properties that are rough approximations and that may have systematic biases. Investigation into a revised expression for the angular location of maximum normal stress is currently underway at MIT.

#### 4.2. Deformable Soil Rover Experiments at the Jet Propulsion Laboratory Mars Yard and the Dumont Dunes, Mojave Desert

The Surface System Test Bed (SSTB-Lite) rover is a 3/8 mass (65.5 kg vs 176.5 kg) version of the two MERs used for various field tests focused on mobility. This mass ratio was chosen so that the terrestrial wheel load for SSTB-Lite is approximately the same as the load on Mars. Numerous SSTB-lite tests were conducted at the JPL Mars Yard on soil-covered surfaces with varying slopes. A main conclusion was that the rover could climb slopes as high as  $\sim 20^\circ$  before the wheels attained 90% slip values (Lindemann et al., 2006). The soil simulant for these tests was poorly sorted angular river sand. Unfortunately, wheel sinkage was not measured, so it is impossible to model compaction resistance and thus other parameters using Artemis. To increase understanding of SSTB-Lite's slope climbing abilities and to provide data to compare to Artemis simulations, the rover was deployed to the Dumont Dunes in the Mojave Desert, CA, in May 2012. The tests were conducted on an interdune area, climbing onto a dune face as shown in Figure 11. The dunes are composed of well-sorted and extremely well-rounded sands, and the expectation was that key parameters related to slip should be quite different as opposed to the poorly sorted and angular river sands. Slip was determined by manually measuring the wheel's tie-down cleat imprint separations, as shown in Figure 12. Tie down cleats were included in the wheels as a way to connect the rover to the spacecraft that carried the MERs to Mars. Slip measurement errors estimated to be  $\sim 0.6\%$  were derived from the estimated 0.5 cm accuracy of cleat mark measurements. The average wheel slip was calculated by the following equation:

$$i_{est} = 1 - \frac{d}{2\pi r} \quad (24)$$

where  $d$  is the distance between two tie-down cleat imprints and  $r$  is the wheel radius.

Wheel sinkage was measured indirectly by counting the number of sand-covered wheel cleats using images captured at each slip test location, with resultant relatively large depth measurement errors, particularly at high slope and slip values. Terrain slope values were measured using a digital electronic level which was placed on the SSTB-Lite deck. Because of the small difference in sinkage between the front and back wheels, the measured SSTB-Lite pitch angle also corresponds to the local slope angle. The tests included forward driving uphill and backward driving downhill. The drives exhibited slopes varying from  $2^\circ$  to  $12^\circ$ . Both slip and sinkage measurements were measured for the rear left wheel for the uphill drive and the front left wheel for the downhill drive (Figures 13 and 14).

Artemis simulations of the drives used soil bulk density values measured on-site by collecting an undisturbed volume of sand of known quantity and weighing it. This value is reported in Table II, along with other estimates of the required terramechanics parameter values. Cohesion and the angle of internal friction were derived from the literature for loose dune sands with a slight amount of moisture. Values for the pressure-sinkage relationship were initially derived from MIT test-bed pressure-sinkage parameters for the Mojave Mars Simulant and then tuned to fit the sinkage range. The soil rebound ratio, as well as values of  $a_1$  and  $a_2$ , which are from Oida et al. (1991) for cohesiveless dry sand, were also fixed in these Artemis runs. The remaining parameters ( $k_x$  and  $n_1$ ) were tuned to match the data, in this case measured slip values as a function of slope. Unfortunately, SSTB-Lite was not instrumented to determine wheel torques or drawbar pull values, so these values could not be compared to model results. Finally, visual monitoring of the tracks produced by the leading and middle wheels during the uphill drive showed that the rear wheels produced the only measurable sinkage, whereas only the front wheels left a discernible track during the downhill drive. Thus multipass effects were not incorporated into the Artemis models for the drives.

Model results with and without slip-sinkage are plotted in Figures 13 and 14 and are based on final soil parameters listed in Table II. The chi square analysis only used slip as a function of slope because of the large uncertainties in determining sinkage values. The tuned value for  $k_x$  is much larger as compared to its initial value but still within

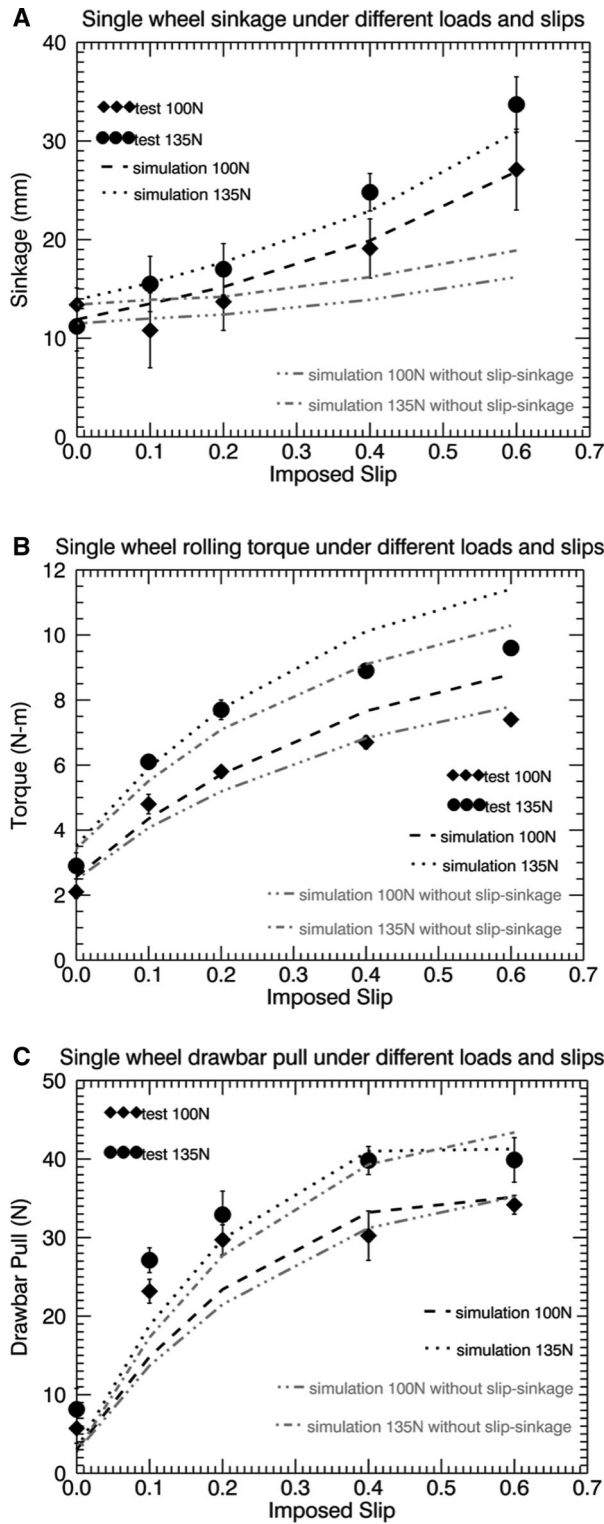


Figure 10. MER single-wheel comparison between tests and simulations.

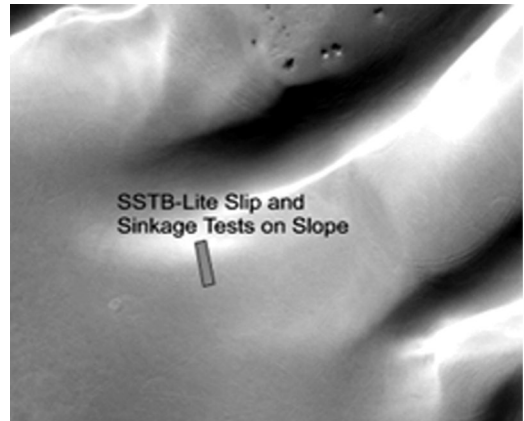


Figure 11. SSTB-Lite test site, Dumont Dunes, Mojave Desert, CA.



Figure 12. SSTB-Lite wheel slip measurement.

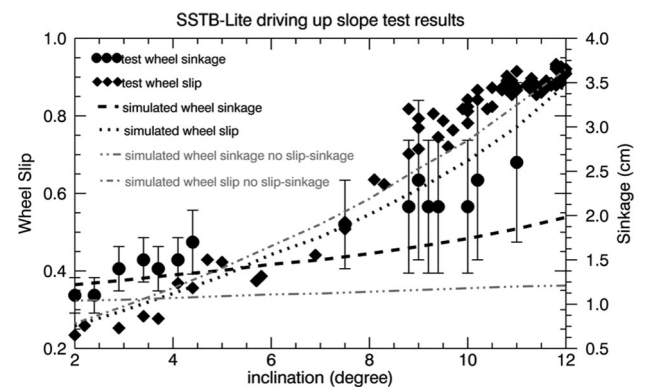
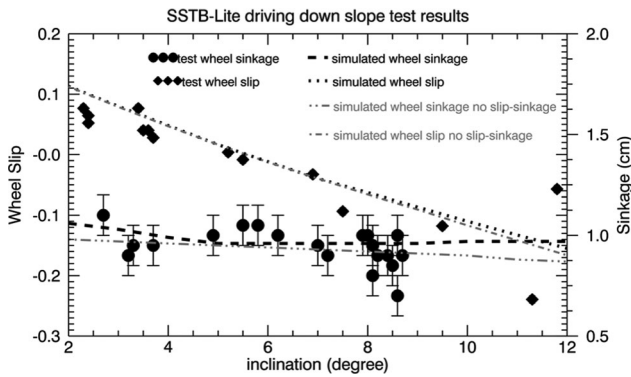


Figure 13. Observed and simulated SSTB-Lite rear left wheel slip and sinkage along slopes for the forward uphill drive.

reported ranges in the literature (Ishigami, 2008), and this value is not surprising considering the well-rounded and well-sorted sands (i.e., high  $k_x$ ) that dominate the Dumont Dunes. This result is also consistent with the much higher slip values for the dune sands as opposed to the tests in



**Figure 14.** Observed and simulated SSTB-Lite front left wheel slip and sinkage along slopes for the backward downhill drive.

river sands (poorly sorted and angular and more likely to engender more grip for drive wheels) conducted at the JPL Mars Yard and reported in Lindemann et al. (2006).

Slip-sinkage effects are predicted to have a significant impact on wheel sinkage for the uphill drive, as shown in Figure 13. The reason is that the load and thus compaction resistance increased on the downhill wheel as slope increased. The increased thrust needed to achieve commanded angular velocities caused increased slip and slip-sinkage. Counterintuitively, simulated slip values that do not include slip-sinkage effects are higher than the values that include slip-sinkage (Figure 13). Exploration of model results shows that this is because of less sinkage without slip-sinkage effects, thereby less contact area between the wheel and soil, and increased wheel slip as the wheels tried to reach commanded angular velocities. The downhill drive simulation predicts the range of skid measured for the wheel, the shift to slip at low slope angles, and the relatively low sinkage associated with the uphill wheel, increasing as the slope decreased and that wheel started to carry more of the rover load (Figure 14). The model also predicts a minimum value of sinkage between 5° and 6° slope associated with the transition from skid to slip, although the sinkage data are not of high enough fidelity to confirm this minimum. In summary, comparisons between the data and Artemis simulations again provide physical insight into the behavior of the rover in the dune sands, although mea-

surement inaccuracies preclude rigorous evaluation of the extent to which Artemis simulates all aspects of the drives and allows retrieval of accurate sand properties.

### 4.3. Simulation of Opportunity's Ripple Crossing on Sol 2143

On Sol 2143 (i.e., 2,143 Mars days after landing), Opportunity was commanded to traverse a 5-m-wide and 0.4-m-high wind-blown sand ripple (Arvidson et al., 2011b). The flanks of the ripple included thin soil over bedrock. To prepare for the crossing, the rover was first commanded to perform a 2 m rear drive, followed by an arc-turn drive to orient the rover to drive backward directly across the ripple, and then a backward drive across the ripple. The backward drive was commanded because the steering actuator of Opportunity's right front wheel failed early in the mission and the wheel was permanently left turned inward by ~8°. Driving backward produced less turning about this wheel as compared to forward driving. Generally, for the straight drive on a flat surface, commanded wheel angular velocity is 17 deg/s and rover velocity is around 3.89 cm/s. The actual rover velocity and wheel angular rate may vary from time to time, depending on the actual command and drive types. Figure 15 shows Navcam views of the ripple and wheel tracks after the drive, and the terrain surface as a perspective diagram is shown in Figure 16.

Total wheel sinkage (i.e., after the third wheel pair pass) as a function of location for the ripple traverse was determined from differential comparisons of Navcam-based digital elevation models acquired before and after crossing the ripple. The data are shown in Figure 17. Examination of the scatter in the retrieved track depths suggests a vertical sinkage error of ~1 cm. Wheel slippage was determined using visual odometry for 13 stops along the traverse, and data are shown in Figure 17, with locations retrieved from rover clock times using the slip values for corrections. Finally, Figure 18 shows the rover pitch values along the traverse determined from onboard accelerometers, again adjusted from rover clock to distance values using slip determined from visual odometry. The ensemble of data shows that Opportunity began and ended its ripple crossing on bedrock thinly covered by soil, producing low sinkage and slip values at the beginning of the traverse while the vehicle pitch (along

**Table II.** Soil parameters for modeling SSTB-Lite Dumont Dunes tests.

	$\rho$	$c$	$\phi$	$k'_c$	$k'_\phi$	$n(n_0)$	$n_1$	$k_x$	$a_1$	$a_2$	Rebound
unit	kg/m <sup>3</sup>	kPa	deg	-	-	-	-	mm	-	-	-
initial	1650	0.2	30	677.5	212.2	1.4	0.32	12	0.33*	0.11*	5%
final	1650	0.2	30	9.1	500.8	1.4	0.45	29	0.33*	0.11*	5%

Note:  $a_1, a_2$  from Oida et al. (1991) for cohesiveless dry sand;  $c, k_x,$  and  $\phi$  from Ding et al. (2009) and Scharringhausen et al. (2009); sinkage parameters from MIT test-bed soil parameters (Table I). Soil rebound ratio is set as a constant.

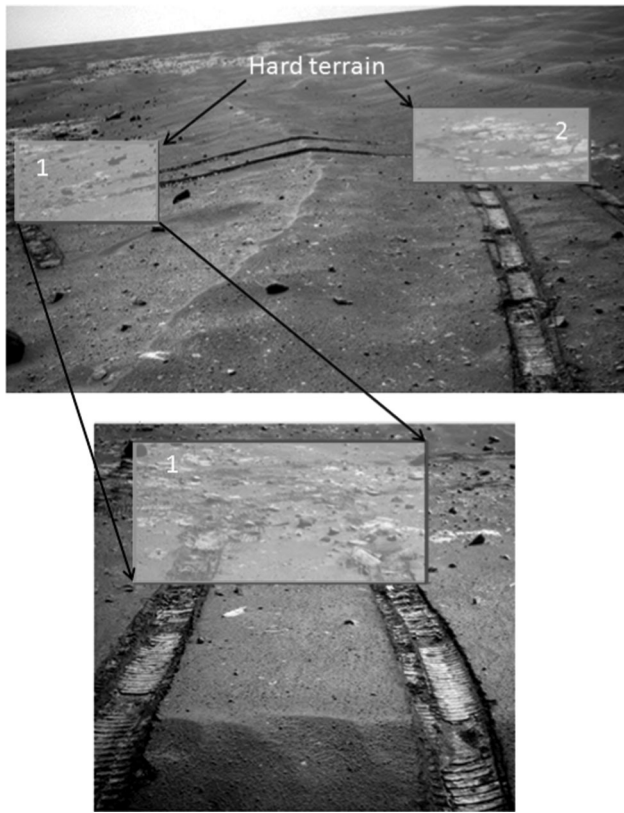


**Figure 15.** Navcam images acquired after the ripple crossing on Sol 2143. Boxes 1 and 2 denote the beginning and ending part of the ripple crossing drive, respectively, where thin soil overlies bedrock. The top Navcam image is 1N318788123EFFABCRP1905L0M1 acquired after Opportunity drove along the interrubble area, and the bottom Navcam image is 1N318433348EFFABAPP1764L0M1 acquired just after the crossing and looking back along the drive direction.

its drive direction) was low (Figure 19). Increasing pitch as the rover climbed the ripple corresponds to increased sinkage and slip, whereas the downhill component produced less sinkage and slip as pitch decreased, with the slip converting to skid as the rover became tilted in a downhill direction. The last portion of the drive led to an increasing pitch value as the rover crossed the interrubble region. Clearly the drive encountered two types of surfaces. The first corresponded to the thin soil over bedrock on the ripple flanks and interrubble terrain, and the second to the deformable soil associated with the aeolian ripple. Detailed examination of similar ripple soils by Opportunity showed that this material is composed of poorly sorted basaltic sands mixed with wind-blown dust (Arvidson et al., 2011b).

The first step in simulating the ripple traverse was to replicate the sinkage as a function of pitch using the pressure-sinkage relationship. This provided the needed

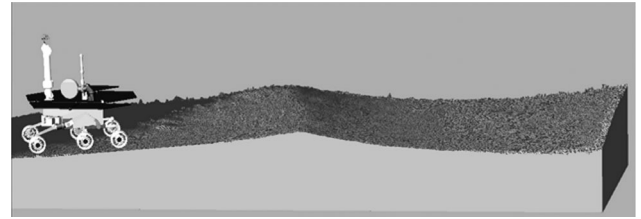


**Figure 16.** Sol 2143 ripple crossing simulation with Artemis. The modeled surface is 10 m long and the ripple is approximately 0.40 m high and was derived from a Navcam-based digital elevation model.

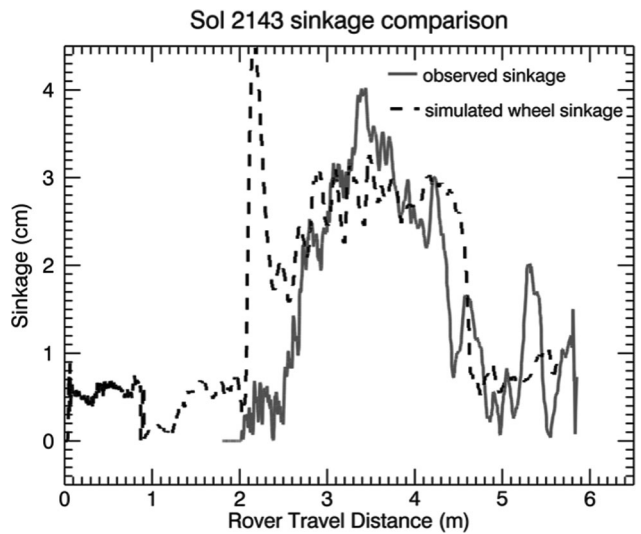


**Figure 17.** Simulated and observed Opportunity wheel sinkage after the three wheels passed through the traverse. Model bump at ~2.1 m is associated with passage over a pair of rocks.

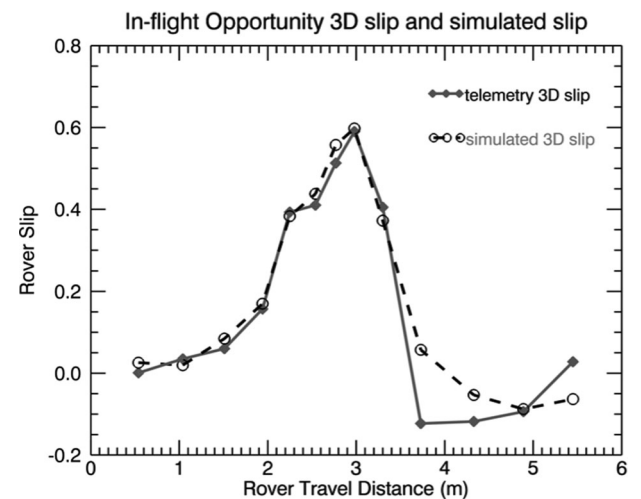


**Figure 18.** Telemetry 3D slip comparing to simulated slip on Sol 2143 with multiple soil regions.

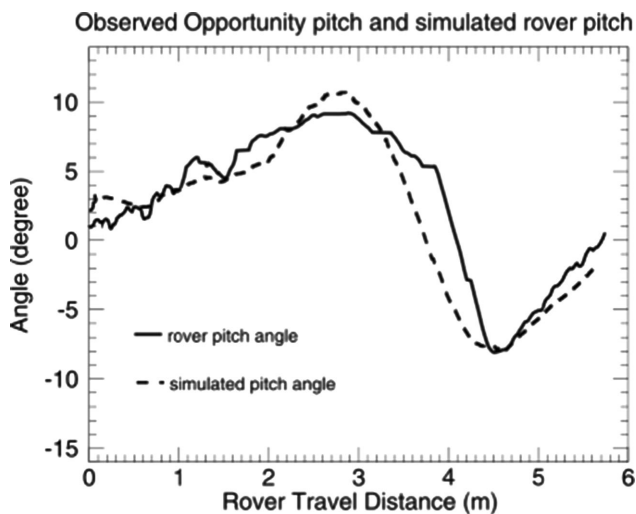


**Figure 19.** Simulated and observed pitch angle of Opportunity.

information on relevant constants (Table III) and thus compaction resistances. Values for soil bulk density, cohesion, and angle of internal friction were adopted from the literature for Martian wind-blown (for the ripple) and crusted soils (to mimic thin soil over bedrock) (Herkenhoff et al., 2008; Moore, Clow, Hutton, & Spitzer, 1987; Sullivan, Anderson, Biesiadecki, Bond, & Stewart, 2011) (Table III). The multipass effect was modeled in this simulation with coefficients  $k_1$  and  $k_2$  derived from Senatore and Sandu (2011) given initial slip at 0.3 (Table III). Initial pressure-sinkage constants were derived from the Dumont Dunes, adjusted for soil weight density, and then tuned to match the observed sinkages shown in Figure 17. Other parameters were then tuned to match observed slip values as a function of rover pitch using chi square minimization, and it was found that  $k_x$  controlled most of the variance between model and data. Final values for all parameters are shown in Table III.

The model results best fit slip as a function of rover pitch, which is not surprising given that the model was tuned to best match these data sets. Both the sign and magnitude of slip are reasonably well-simulated. Total sinkage due to passage of the three wheels shows minimal values for the hard terrain on either side of the ripple and higher sinkage values on the ripple. The outcome is similar to what was found for both the MIT and Dumont data and model results in that Artemis provides physical insight into the observed behavior of the rover and how it interacts with terrain elements.

#### 4.4. Drives at Greeley Winter Haven

Opportunity is solar-powered, and because of the continued accumulation of wind-blown dust on the solar panels, the vehicle was placed on a northerly tilted ( $15^\circ$ ) bedrock

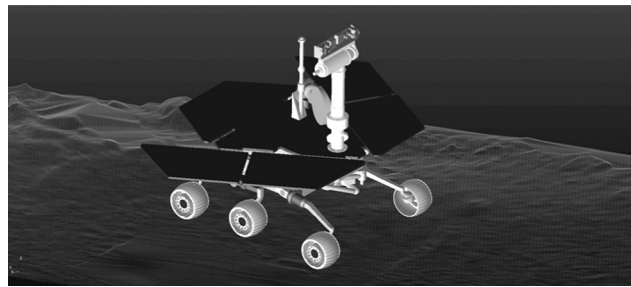


**Figure 20.** Opportunity is shown tilted approximately 15 degrees on a digital elevation model extracted from Navcam stereo images. The bumpy terrain mesh reflects the irregular bedrock surface.

surface to survive the southern hemisphere winter season (Figure 20). This site, named Greeley Winter Haven, on the northern side of Cape York, is an impact breccia outcrop with a highly irregular surface. On Sol 2808, Opportunity was commanded to drive forward and then turn-in-place to orient the rover for further deployment of its robotic arm for in situ measurements. Visual odometry was used to perform these short drives to ensure motions to the exact location for in situ work. Limits were set on wheel drive actuator currents to ensure a safe set of motions on this irregular surface. In fact, the drive stopped when currents on the right front wheel exceeded set threshold values during the turn-in-place phase of the motions. Before the turn-in-place, currents for all wheel drive actuators averaged approximately 0.25 A, whereas during the turn the right front wheel drive actuator current increased to 0.6 A, and then to 1.1 A, whereas the other wheels stayed at relatively low values. The increase in current caused the drive to automatically stop because a current threshold was reached. A possible reason discussed by the rover engineers for the current increase was because the wheel became stuck on an underlying rocky fragment. To better understand the actual underlying cause of this anomaly, an Artemis bedrock model was used to simulate the drive segments to provide a simpler explanation for the increased current supplied to the right front wheel drive actuator. Note that conversion from current to torque is problematical for the MER because of limited calibration information and actuator temperature measurements.

Parameters used in the wheel-bedrock contact model are listed in Table IV and are typical values used in standard Adams contact models. The use of standard values was deemed acceptable because, again, the model was being used to provide physical insight into the drive and was not expected to yield highly precise numerical simulation results. The model run showed that the high currents on the right front wheel can simply be explained as a consequence of more weight on that wheel, and a stickslip wheel-rock

**Table III.** Estimated parameters for multiple soil simulation on Sol 2143.

soil	$\rho$	$c$	$\phi$	$k'_c$	$k'_\phi$	$n_0$	$n_1$	$k_x$	$a_1$	$a_2$	$k_1$	$k_2$
unit	kg/m <sup>3</sup>	kPa	deg	-	-	-	-	mm	-	-	-	-
1	1600	1.5	35	100	1000	1.1	0.1	15	0.33	0.11	1.154	0.0348
2	1300	0.25	30	10	500	1.4	0.18	25	0.32	0.20	1.154	0.0348
3	1600	2.5	35	100	1000	1.1	0.1	12	0.33	0.11	1.154	0.0348

Note:  $a_1, a_2$  from Oida et al. (1991) for cohesiveless dry sand; multipass coefficients  $k_1, k_2$  are based on Senatore and Sandu (2011) derived from 0.3 slip value; soil rebound ratio is set as a constant (5%) using Dumont Dunes data.

**Table IV.** Bedrock friction parameters and nominal values.

Frictional parameters	Description	Unit	Nominal Value
$k$	material stiffness between wheel and bedrock	N/m <sup>e</sup>	7.53E+007
$e$	exponent of the force deformation characteristic	-	2.0
$c_{max}$	maximum damping coefficient between wheel and bedrock	kg/s	8140.0
$z_{max}$	maximum penetration	m	0.002
$\mu_s$	static friction coefficient between wheel and bedrock	-	0.757
$\mu_d$	dynamic friction coefficient between wheel and bedrock	-	0.597
$v_{st}$	stiction transition velocity	m/s	0.03
$v_{ft}$	friction transition velocity	m/s	0.05

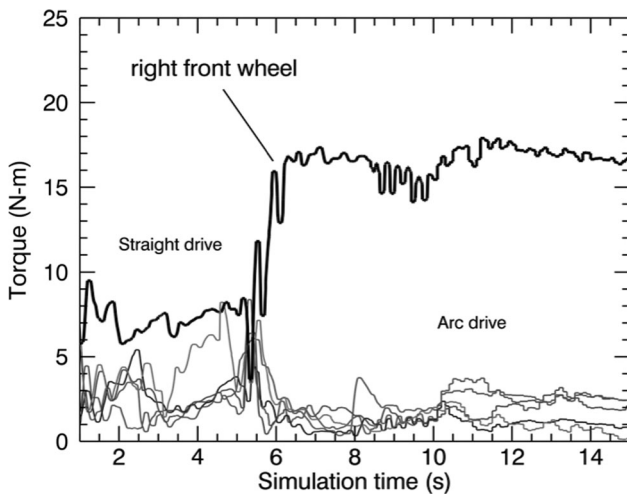


**Figure 21.** Simulated torque for each wheel on the Sol 2808 drive simulation.

interaction on the irregular outcrop. The other wheels could not provide sufficient thrust to move the vehicle. Because of its higher load, the right front wheel attempted to draw a higher current to achieve its commanded angular velocity, but reached the current limit (represented as an increased torque in Artemis, Figure 21). Based on the results of the simulation, the rover planners were able to confidently plan a maneuver for Opportunity to move it back to a higher tilt to survive the winter season.

## 5. CONCLUSIONS AND FUTURE WORK

The development and implementation of Artemis, a rover-based simulator for driving across realistic terrains with deformable soils or bedrock surfaces, were described in this paper. Artemis developments have focused on models for the Mars Exploration Rovers (MERs), Spirit and Opportunity, and the Mars Science Laboratory, Curiosity, although only the MER development was covered in this paper. An evaluation of the capabilities and limitations for the use of Artemis was presented, including single wheel tests in deformable soils using an MER wheel, MER rover-scale tests at the JPL Mars Yard, and at the Dumont Dunes in the Mojave Desert. Applications to Opportunity flight data were summarized, including a traverse across an aeolian ripple on the Meridiani plains and a drive on a tilted bedrock surface in Cape York. Results indicate that Artemis is capable of providing significant insight into the behavior of the rovers as they cross realistic terrains and the physics underlying the responses. Limitations are also evident, largely because of limitations in the use of the classical terramechanics equations for how wheels interact with deformable soils. Artemis will continue to evolve, including replacement of the wheel-soil contact model with more modern approaches (e.g., use of discrete element models). Further validation of Artemis is also planned using laboratory and field-based tests, and the model will be compared to archival flight data for Spirit, Opportunity, and Curiosity drives. The intent is to develop and implement a validated model that can be used in a predictive manner for safe path planning and, eventually, retrieval of terrain properties.

## ACKNOWLEDGMENTS

This research is funded by a contract to Washington University for the NASA Mars Exploration Rover Mission. This work is also supported in part by the W.M. Keck Institute for Space Studies. Part of this research was carried out at the Jet Propulsion Laboratory, California Institute of Technology, under a contract with the National Aeronautics and Space Administration. The authors thank PDS Geosciences Node for providing image data. Navcam images used in this paper can be found in (<http://an.rsl.wustl.edu/mer/merbrowser/browserFr.aspx?tab=search&m=MERB>).

## REFERENCES

- Abebe, A., Tanaka, T., & Yamazaki, M. (1989). Soil compaction by multiple passes of a rigid wheel relevant for optimization of traffic. *Journal of Terramechanics*, 26(2), 139–148.
- Adams online help (2012). Online help document available online: <http://simcompanion.mscsoftware.com/infocenter/index?page=content&cat=1VMO50&channel=documentation>, last accessed April 7th, 2013.
- Arvidson, R., Squyres, S., Anderson, R., Bell III, J., Blaney, D., Brückner, J., et al. (2006). Overview of the Spirit Mars Exploration Rover Mission to Gusev Crater: Landing site to Backstay Rock in the Columbia Hills. *Journal of Geophysical Research*, 111, E02S01, doi: 10.1029/2005JE002499.
- Arvidson, R., Ruff, S., Morris, R., Ming, D., Crumpler, L., Yen, A., et al. (2008). Spirit Mars Rover Mission to the Columbia Hills, Gusev Crater: Mission overview and selected results from the Cumberland Ridge to Home Plate. *Journal of Geophysical Research*, 113, E12S33, doi: 10.1029/2008JE003183.
- Arvidson, R., Bell III, J., Bellutta, P., Cabrol, N., Catalano, J., Cohen, J., et al. (2010). Spirit Mars Rover Mission: Overview and selected results from the northern Home Plate winter haven to the side of Scamander Crater. *Journal of Geophysical Research*, 115, E00F03, doi:10.1029/2010JE003633.
- Arvidson, R., Ashley, J., Bell III, J., Chojnacki, M., Cohen, J., Economou, T., et al. (2011a). Opportunity Mars Rover Mission: Overview and selected result from Purgatory Ripple to traverses to Endeavour Crater. *Journal of Geophysical Research*, 116, E00F15, doi:10.1029/2010JE003746.
- Arvidson, R., Van Dyke, L., Bennett, K., Zhou, F., Iagnemma, K., Senatore, C., et al. (2011b). Mars Exploration Rover Opportunity terramechanics across ripple covered bedrock in Meridiani Planum. Abstract at 2011 42nd Lunar and Planetary Science Conference, The Woodlands, TX, available online: <http://www.lpi.usra.edu/meetings/lpsc2011/pdf/1503.pdf>, last accessed on April 7th, 2013.
- Arvidson, R., Fuller, D., Heverly, M., Iagnemma, K., Lin, J., Matthews, J., et al. (2013). Mars Science Laboratory Curiosity Rover terramechanics initial results. Abstract at 2013 44th Lunar and Planetary Science Conference, The Woodlands, TX, available online: <http://www.lpi.usra.edu/meetings/lpsc2013/pdf/1193.pdf>, last accessed on April 7th, 2013.
- AS2TM (2003). Matlab/Simulink Module AS2TM User's Guide, version 1.12, available online: <http://www.tire-soil.de/Demo/Version-1.13/UserGuide.pdf>, last accessed on April 7th, 2013.
- Bauer, R., Leung, W., & Barfoot, T. (2005). Development of a dynamic simulation tool for the Exomars rover. Paper presented at the 8th International Symposium on Artificial Intelligence, Robotics and Automation in Space, Munich, Germany.
- Bekker, M. (1960). Off-the-road locomotion; research and development in terramechanics. Ann Arbor: The University of Michigan Press.
- Bekker, M. (1969). Introduction to terrain-vehicle systems. Ann Arbor: The University of Michigan Press.
- Benamar, F., & Grand, C. (2013). Quasi-static motion simulation and slip prediction of articulated planetary rovers using a kinematic approach. *Journal of Mechanisms and Robotics*, 5(2), 021002(1–13), doi: 10.1115/1.4023873.
- Biesiadecki, J., Baumgartner, E., Bonitz, R., Cooper, B., Hartman, F., Leger, P., et al. (2006). Mars Exploration Rover surface operations: Driving Opportunity at Meridiani Planum. *Robotics & Automation Magazine, IEEE*, 13(2), 63–71.
- Biesiadecki, J., Leger, P., & Maimone, M. (2007). Tradeoffs between directed and autonomous driving on the Mars Exploration Rovers. *The International Journal of Robotics Research*, 26(1), 91–104.
- Cameron, J., Jain, A., Huntsberger, T., Sohl, G., & Mukherjee, R. (2009). Vehicle-terrain interaction modeling and validation for Planetary Rovers. JPL Publication 10–15, available online: <http://hdl.handle.net/2014/41675>, last accessed on April 7th, 2013.
- Cheng, Y., Maimone, M., & Matthies, L. (2006). Visual odometry on the Mars Exploration Rover. *Robotics & Automation Magazine, IEEE*, 13(2), 54–62.
- Coduto, D. (2001). *Foundation design: Principles and practices*, 2<sup>nd</sup> ed. New Jersey: Prentice Hall.
- Cowan, D., & Sharf, I. (2007). Dynamics modeling and traction control for Mars rovers. Paper presented at 58th International Astronautical Congress, Hyderabad, India.
- Del Rosario, C. (1980). Lateral force investigations on steered, pneumatic tyres operating under soil conditions. Ph.D. thesis, Silsoe College, Cranfield Institute of Technology, UK.
- Ding, L., Yoshida, K., Nagatani, K., Gao, H., & Deng, Z. (2009). Parameter identification for planetary soil based on a decoupled analytical wheel-soil interaction terramechanics model. Paper presented at the 2009 IEEE International Conference on Intelligent Robots and Systems, St. Louis, MO.
- Ding, L., Gao, H., Deng, Z., & Tao, J. (2010a). Wheel slip-sinkage and its prediction model of lunar rover. *Journal of Central South University of Technology*, 17, 129–135.

- Ding, L., Nagatani, K., Sato, K., Mora, A., Yoshida, K., Gao, H., & Deng, Z. (2010b). Terramechanics-based high-fidelity dynamics simulation for wheeled mobile robot on deformable rough terrain. Paper presented at 2010 IEEE International Conference on Robotics and Automation, Anchorage, AK.
- Dupont, P., & Yamajako, S. (1997). Stability of frictional contact in constrained rigid-body dynamics. *IEEE Transactions on Robotics and Automation*, 13(2), 230–236.
- Fervers, C. (2004). Improved FEM simulation model for tire-soil interaction. *Journal of Terramechanics*, 41(2), 87–100.
- Golombek, M., Cook, R., Economou, T., Folkner, W., Haldemann, A., Kallemeyn, P., et al. (1997). Overview of the Mars Pathfinder Mission and Assessment of Landing Site Predictions. *Science*, 278, 1743–1748.
- Grotzinger, J., Crisp, J., Vasavada, A., Anderson, R., Baker, C., Barry, R., et al. (2012). Mars Science Laboratory mission and science investigation. *Space Science Reviews*, 170, 5–56, doi: 10.1007/s11214-012-9892-2.
- Grotzinger, J., Blake, D., Crisp, J., Edgett, K., Gellert, R., Gomez-Elvira, J., et al. (2013). Mars Science Laboratory: First 100 sols of geologic and geochemical exploration from Bradbury Landing to Glenelg. Abstract at 2013 44th Lunar and Planetary Science Conference, The Woodlands, TX, available online: <http://www.lpi.usra.edu/meetings/lpsc2013/pdf/1259.pdf>, last accessed on April 7th, 2013.
- Hegedus, E. (1960). A simplified method for the determination of bulldozing resistance. Land Locomotion Research Laboratory, Army Tank Automotive Command Report, 61.
- Herkenhoff, K., Golombek, M., Guinness, E., Johnson, J., Kuskack, A., Richter, L., et al. (2008). In situ observations of the physical properties of the Martian surface. In J. Bell (Ed.): *The Martian surface*. Cambridge University Press.
- Hettiaratchi, R., & Reece, A. (1967). Symmetrical three-dimensional soil failure. *Journal of Terramechanics*, 4(3), 45–76.
- Holm, I. (1969). Multi-pass behaviour of pneumatic tires. *Journal of Terramechanics*, 6(3), 47–71.
- Horner, D., Peters, J., & Carrillo, A. (2001). Large scale discrete element modeling of vehicle-soil interaction. *Journal of Engineering Mechanics*, 127(10), 1027–1032.
- Iagnemma, K., Senatore, C., Trease, B., Arvidson, R., Shaw, A., Zhou, F., et al. (2011). Terramechanics modeling of Mars surface exploration rovers for simulation and parameter estimation. Paper presented at the ASME Design Engineering Technical Conference, Washington, DC.
- Inotsume, H., Sutoh, M., Nagaoka, K., Nagatani, K., & Yoshida, K. (2012). Slope traversability analysis of reconfigurable planetary rovers. Paper presented at IEEE/RSJ International Conference on Intelligent Robots and Systems (IROS), Algarve, Portugal.
- Ishigami, G., Miwa, A., Nagatani, K., & Yoshida, K. (2006, June). Terramechanics-based analysis on slope traversability for a planetary exploration rover. Paper presented at the 25th International Symposium on Space Technology and Science, Kanazawa, Japan.
- Ishigami, G., Miwa, A., Nagatani, K., & Yoshida, K. (2007). Terramechanics-based for steering maneuver of planetary exploration rovers on loose soil. *Journal of Field Robotics*, 24(3), 233–250.
- Ishigami, G. (2008). Terramechanics-based analysis and control for lunar/planetary exploration robots. Ph.D. thesis, Tohoku University, Sendai, Japan.
- Janosi, Z., & Hanamoto, B. (1961). Analytical determination of drawbar pull as a function of slip for tracked vehicles in deformable soils. Paper presented at the 1st International Conference on Terrain-Vehicle Systems, Turin, Italy.
- Knuth, M., Johnson, J., Hopkins, M., Sullivan, R., & Moore, J. (2012). Discrete element modeling of a Mars Exploration Rover wheel in granular material. *Journal of Terramechanics*, 49(1), 27–36.
- Krenn, R., & Hirzinger, G. (2008). Simulation of rover locomotion on sandy terrain-modeling, verification and validation. Paper presented at the 10th Workshop on ASTRA, Noordwijk, The Netherlands.
- Krenn, R., & Hirzinger, G. (2009). SCM—A soil contact model for multi-body system simulations. Paper presented at the 11th European Regional Conference of the International Society for Terrain-Vehicle Systems, Bremen, Germany.
- Kraus, P., Kumar, V., & Dupont, P. (1998). Analysis of frictional contact models for dynamic simulation. Paper presented at the 1998 IEEE International Conference on Robotics and Automation, Lueven, Belgium.
- Lindemann, R. (2005). Dynamic testing and simulation of the Mars Exploration Rover. Paper presented at 2005 ASME International Design Engineering Technical Conferences, Long Beach, CA.
- Lindemann, R., & Voorhees, C. (2005). Mars Exploration Rover mobility assembly design, test, and performance. Paper presented at the 2005 IEEE Conf. Syst., Man, Cybern., Waikoloa, HI.
- Lindemann, R., Bickler, D., Harrington, B., Ortiz, G., & Voorhees, C. (2006). Mars Exploration Rover mobility development. *IEEE Robotics & Automation Magazine*, 13(2), 19–26.
- Lyasko, M. (2010). Slip sinkage effect in soil-vehicle mechanics. *Journal of Terramechanics*, 47(1), 21–31.
- Maimone, M., Cheng, Y., & Matthies, L. (2007). Two years of visual odometry on the Mars Exploration Rovers. *Journal of Field Robotics*, 24(3), 169–186.
- Moore, H., Clow, G., Hutton, R., & Spitzer, C. (1987). Physical properties of the surface materials at the Viking landing sites on Mars. U.S. Geological Survey Professional Paper, 1389, 222, 1987.
- MSC Software (2012). Adams, available online: <http://www.mscsoftware.com/product/adams/>, last accessed April 7th, 2013.
- Muro, T., & O'Brien, J. (2004). *Terramechanics: Land Locomotion Mechanics*. Taylor & Francis.

- Oida, A., Satoh, A., Itoh, H., & Triratnasirichai, K. (1991). Three-dimensional stress distribution on a tire-sand contact surface. *Journal of Terramechanics*, 28(4), 319–330.
- Peters, G., Abbey, W., Bearman, G., Mungas, G., Smith, J., & Anderson, R. (2008). Mojave Mars simulat—Characterization of a new geologic Mars analog. *Icarus*, 197(2), 470–479.
- Reece, A. (1965). Principles of soil-vehicle mechanics. Paper presented at Proceedings Institution of Mechanical Engineers.
- Richter, L., Ellery, A., Gao, Y., Michaud, S., Schmitz, N., & Weiss, S. (2006). A predictive wheel-soil interaction model for planetary rovers validated in testbeds and against MER Mars rover performance data. Paper presented at the 10th European Conference of the International Society for Terrain-Vehicle Systems (ISTVS), Budapest, Hungary.
- Schäfer, B., Gibbesch, A., Krenn, R., & Rebele, B. (2010). Planetary rover mobility simulation on soft and uneven terrain. *Journal of Vehicle System Dynamics*, 48(1), 149–169.
- Scharringhausen, M., Beermann, D., Krömer, O., & Richter, L. (2009). A wheel-soil interaction model for planetary application. Paper presented at the 11th European Conference of the International Society for Terrain-Vehicle Systems (ISTVS), Bremen, Germany.
- Scholander, J. (1974). Bearing capacity of some forest soils: Some technical aspects and consequences. Garpenberg: Royal School of Forestry.
- Schwanghart, H. (1968). Lateral forces on steered tyres in loose soil. *Journal of Terramechanics*, 5(1), 9–29.
- Senatore, C., & Iagnemma, K. (2011, September). Direct shear behaviour of dry, granular soils for low normal stress with application to lightweight robotic vehicle modeling. Paper presented at the 17th International Conference of the International Society for Terrain Vehicle Systems, Blacksburg, VA.
- Senatore, C., & Sandu, C. (2011). Off-road tire modeling and the multi-pass effect for vehicle dynamics simulation. *Journal of Terramechanics*, 48(4), 265–276.
- Senatore, C., Wulfmeier, M., MacLennan, J., Jayakumar, P., & Iagnemma, K. (2012). Investigation of stress and failure in granular soils for lightweight robotic vehicle applications. Paper presented at the 2012 NDIA Ground Vehicle Systems Engineering and Technology Symposium, Troy, MI.
- Sohl, G., & Jain, A. (2005). Wheel-terrain contact modeling in the roams planetary rover simulation. Paper presented at the 2005 ASME International Design Engineering Technical Conference, Long Beach, CA.
- Song, P., Kraus, P., Kumar, V., & Dupont, P. (2000). Analysis of rigid body dynamic models for simulation of systems with frictional contacts. *Journal of Applied Mechanics*, 68, 118–128.
- Squyres, S., Arvidson, R., Bell III, J., Brückner, J., Cabrol, N., Calvin, W., et al. (2004a). The Spirit Rover's Athena Science Investigation at Gusev Crater, Mars. *Science*, 305, 794–799.
- Squyres, S., Arvidson, R., Bell III, J., Brückner, J., Cabrol, N., Calvin, W., et al. (2004b). The Opportunity Rover's Athena Science Investigation at Meridiani Planum, Mars. *Science*, 306, 1698–1703.
- Squyres, S., Arvidson, R., Bollen, D., Bell III, J., Brückner, J., Cabrol, N., et al. (2006). Overview of the Opportunity Mars Exploration Rover Mission to Meridiani Planum: Eagle Crater to Purgatory Ripple. *Journal of Geophysical Research*, 111, E12S12, doi: 10.1029/2006JE002771.
- Sullivan, R., Anderson, R., Biesiadecki, J., Bond, T., & Stewart, H. (2011). Cohesions, friction angles, and other physical properties of Martian regolith from Mars Exploration Rover wheel trenches and wheel scuffs. *Journal of Geophysical Research*, 116, E02006, doi:10.1029/2010JE003625.
- Tao, J., Deng, Z., Fang, H., Gao, H., & Yu, X. (2006, June). Development of a wheeled robotic rover in rough terrains. Paper presented at the 6th World Congress on Intelligent Control and Automation, Dalian, China.
- Terzaghi, K., Peck, R., & Mesri, G. (1996). Soil mechanics in engineering practice, 3<sup>rd</sup> ed. New York: John Wiley & Sons.
- Trease, B., Arvidson, R., Lindemann, R., Bennett, K., Zhou, F., Iagnemma, K., et al. (2011). Dynamic modeling and soil mechanics for path planning of Mars Exploration Rovers. Paper presented at the ASME Design Engineering Technical Conference, Washington, DC.
- Tsuji, T., Nakagawa, Y., Matsumoto, N., Kadono, Y., Takayama, T., & Tanaka, T. (2012). 3-D DEM simulation of cohesive soil-pushing behavior by bulldozer blade. *Journal of Terramechanics*, 49(1), 37–47.
- Watyotha, C., Gee-Clough, D., & Salokhe, V. (2001). Effect of circumferential angle, lug spacing and slip on lug wheel forces. *Journal of Terramechanics*, 38(1), 1–14.
- Wong, J., & Reece, A. (1967a). Prediction of rigid wheel performance based on the analysis of soil-wheel stresses. Part I. Performance of driven rigid wheels. *Journal of Terramechanics*, 4(1), 81–98.
- Wong, J., & Reece, A. (1967b). Prediction of rigid wheel performance based on the analysis of soil-wheel stresses. Part II. Performance of towed rigid wheels. *Journal of Terramechanics*, 4(2), 7–25.
- Wong, J. (2001). *Theory of Ground Vehicles*, 3<sup>rd</sup> ed. New York: John Wiley & Sons.
- Wong, J. (2010). *Terramechanics and off-road vehicle engineering: Terrain behaviour, off-road vehicle performance and design*, 2<sup>nd</sup> ed. Elsevier.
- Wong, J. (2012). Predicting the performances of rigid rover wheels on extraterrestrial surfaces based on test results obtained on earth. *Journal of Terramechanics*, 49(1):49–61.
- Yong, R., & Fattah, E. (1976). Prediction of wheel-soil interaction and performance using the finite element method. *Journal of Terramechanics*, 13(4), 227–240.
- Yoshida, K., Watanabe, T., Mizuno, N., & Ishigami, G. (2003). Terramechanics-based analysis and traction control of a lunar/planetary rover. Paper presented at the 4th International Conference on Field and Service Robotics, Lake Yamanaka, Japan.